TOPEX/POSEIDON MICROWAVE RADIOMETER (TMR): 1. INSTRUMENT DI3SCRIPTION AND ANTENNA TEMPERATURE CALIBRATION

Christopher S. Ruf[1]
Stephen J. Keihm[2]
Michael A. Janssen[2]

submitted to
IEEE Transactions on Geoscience and Remote Sensing
on
August 30, 1993

1. Department of Electrical Engineering, The Pennsylvania State University, University Park, PA 16802
2. Jet Propulsion Laboratory, California Institute of Technology, Pasadena, CA 91109

ABSTRACT

The TOPEX/Poseidon Microwave Radiometer (TMR) is a 3-frequency radiometer flown on the. TOPEX/Poseidon (T/P) satellite in low Earth orbit. It operates at 18, 21, arid 37 GHz in a nadir only viewing direction which is co-aligned with the 7/P radar altimeters. TMR monitors and corrects for the electrical path delay of the altimeter radar signal due to water vapor and non-precipitating liquid water in the atmosphere. This paper describes the Th4R instrument and the radiometric instrument calibration required to derive antenna temperature (T_A) from the raw digital data, T_A precision of 0.4 K is predicted on orbit in all expected thermal environments, T_A accuracy of 0.5-0.6 K is expected following a post-launch field calibration campaign. When uncertainties related to antenna sidelobe corrections are included, this T_A accuracy yields a brightness temperature accuracy of 0,7-0.8 K. When combined with a path delay retrieval accuracy of 0,9 cm and an error of 0.3 cm due to differences between the TMR and altimeter antenna footprints, this brightness temperature accuracy insures an overall path delay correction accuracy for the altimeters which meets the mission requirements of 1.2 cm.

1. INTRODUCTION

The primary instruments on the TOPEX/Poseidon (T/P) satellite are two radar altimeters, designed to determine the radial distance between the satellite and the ocean surface by a precise measurement of the round trip time of flight of the radar signal, This distance can be translated into a measurement of the sea level along the T/P ground track given accurate knowledge of the location of the satellite in earth orbit. The nominal satellite altitude of 1375 km and orbit repeat time of 9.9 days result in a

global map of the sea level on a grid spaced 316 km apart at the equator and updated every 9.9 days [1].

A, Radar altimeter errors

There are three general categories of uncertainties associated with the T/P maps of sea level. The first involves the Precision Orbit Determination (POD) algorithm, which locates the spacecraft center of mass relative to a reference Earth geoid. Errors with the POD include inaccuracies in the orbital gravity field, along with a number of other smaller unknowns. Another category of errors involves the inaccuracies of the radar measurements themselves, Radar errors include electronic noise from sources such as time sampling, digitization, and the noise figure of the radar receiver and drifts in instrumental bias. The third category of errors involves inaccuracies in the correction of the time of flight of the radar signal due to propagation effects. The ionosphere, dry air in the atmosphere, and water vapor, primarily in the troposphere, will all delay the radar signal, relative to its time of flight in a vacuum,

A correction is made for the ionospheric delay by using two radar frequencies, at 5,3 and 13.6 GHz, which are affected differently. The integrated free electron content beneath the satellite can be estimated from the difference in time of flight at the two frequencies [2]. The dry atmosphere delay can be estimated from interpolated grids of global surface barometric pressure which are available, e.g. from the Fleet Numerical Oceanography Center (FNOC) [3]. The delay introduced by water vapor is determined from direct TOPEX/Poseidon Microwave Radiometer (TMR) measurements of the integrated water vapor content lying between the spacecraft and the Earth surface [4], The apparent increase in path length due to the water

vapor, relative to propagation in dry air, typically ranges from 5-10 cm in cold, dry climates to 30-50 cm under warm, humid conditions, This effect will henceforth be referred to as the wet tropospheric *path delay*. The uncertainty in sea level due to atmospheric water vapor should be less than 1.2 cm.

B. Previous wet tropospheric path delay corrections

Other satellite altimeters have all attempted to correct for the path delay due to water vapor. The SeaSat radar altimeter operated in conjunction with the Scanning Multichannel Microwave Radiometer (SMMR) [5], In this case, the altimeter's radar signal propagated in the nadir direction, whereas the SMMR antenna was directed 42° away from nadir [6]. Thus, while SMMR was estimated to retrieve nadir normalized path delay with a precision of 1.S cm along its line of propagation [7], the error in its path delay retrieval relative to the actual line of propagation of the radar signal is estimated at 2.5 cm [8]. The GEOSAT altimeter has no companion microwave radiometer and must rely on other estimates of the the wet tropospheric path delay. For example, tropical climatology records compiled from SMMR data show typical monthly standard deviations in the path delay of 1,5-2.5 cm about monthly averages made over several years [9]. However, monthly standard deviations during the El Nino-Southern Oscillation event in 1982-1983 exceeded 12 cm [9] and typical variations on time scales of shorter than one month should exceed the 1.5-2.5 cm. Another option for correction of GEOSAT data makes use of the PERIDOT climatological model of the French Meteorologic Nationale [10]. PERIDOT combines observations and numerical weather prediction models to generate temperature and humidity estimates on a 40 km grid with 15 vertical cells across the Northeast Atlantic and European coast, The accuracy of PERIDOT wet tropospheric path delay retrievals is estimated at 10% of the path

delay [10]. This corresponds to 1-2 cm under typical conditions, but would degrade significantly in high humidity or anomalous weather, The ERS-1 satellite is instrumented with both a radar altimeter and a nadir viewing microwave radiometer. The radiometer operates at 23.8 and 36.S GHz and the accuracy of its wet tropospheric path delay retrieval is estimated to be 2 cm [11].

The above examples illustrate the difficulty of achieving a 1,2 cm accuracy in the wet tropospheric path delay correction. A dedicated microwave radiometer is needed, co-aligned with the radar altimeter antenna and operating at frequencies which optimize the retrieval of atmospheric water vapor. For this reason, the T/P project incorporated TMR into its mission design.

C. *Outline of paper* TMR is a modified version of the SMMR instrument. A full description of SMMR is available in Njoku *et al*. [6], Njoku *et al*. [12], and Swanson and Riley [13]. The hardware modifications for TMR were motivated in part by the change in mission objectives of T/P and in part by calibration problems that SMMR encountered on orbit [14, 15], Part I of this paper begins with a brief description of SMMR, followed by a review of the calibration problems it encountered. Part II follows with a detailed description of the modifications for TMR. In summary, the hardware modifications include: 1) The removal of all antenna scanning hardware; 2) A reduction in the number of operating frequencies, eliminating both polarization channels at 6.6 and 10,7 GHz and one polarization channel at 18 and 37 GHz and leaving one polarization channel each at 18, 21, and 37 GHz for nominal operation and the other polarization channel at 21 GHz as a backup; 3) A redesign of the antenna feed to optimize performance for the remaining channels; 4) The inclusion of

radomes over both the feed and cold sky calibration horns (sky horns); and 5) The selection of a sky horn location and pointing geometry to eliminate direct sun contamination. Part 11 concludes with a summary of the error budget for the retrieval of wet tropospheric path delay by TMR.

Part 111 describes the radiometric instrument calibration required to derive antenna temperature (T_A) from the raw digital data. This procedure is referred to as T_A calibration. The section begins with a description of the T_A calibration approach used by TMR. This approach is a modification to the similar approach which was used with SMMR and which is described in detail by Swanson and Riley [13]. Next, results of the pre-launch calibration and validation of the T_A algorithm are presented which were performed during thermal/vacuum (T/V) testing. The final step in the T_A calibration involves a post-launch calibration and validation program which uses underflight measurements of downwelling brightness temperature and surface meteorology at selected island sites to verify the T_A calibration and "fine tune" the overall TMR wet tropospheric path delay retrieval algorithm. This program is briefly reviewed here in the context of the T_A calibration algorithm. It will be described in much greater detail in an upcoming paper addressing TMR in-flight performance.

II. INSTRUMENT DESCRIPTION

A. Review of the SMMR instrument and its calibration

The SMMR instrument was designed as a multi-spectral microwave imager. It operated at frequencies of 6.6, 10.7, 18,0, 21.0, and 37.0 GHz with channels at both horizontal and vertical polarization. Imaging was performed by a mechanically scanned antenna which rotated about the spacecraft (s/c)

nadir with a constant incidence angle on the Earth of 49°. The antenna design was an offset reflector with a projected aperture diameter of 79 cm and a single multi-frequency feed horn (MFFH) at the prime focus which had output ports at all frequencies and polarizations. 'l'he offset reflector was supported above the MFFH by a set of six graphite epoxy rods which were attached to a ring running around the base of the MFFH at one end and to the outer edge of the reflector at the other end, The radiometer design used a super-heterodyne Dicke approach for all channels,

T_A calibration for SMMR was performed by measuring the radiometer response to hot and cold reference T_As at regular intervals during operation. A microwave ferrite switch matrix between the output port from the MFFH and the input to the Dicke radiometer selected the input source from between the MFFH, a blackbody waveguide termination, and a sky horn, The sky horns used a corrugated feed horn design, with half power beam widths (HPBWs) of approximately 24° at all frequencies. Each sky horn was separated from the actual ferrite switch matrix by a run of waveguide which allowed the horns an unobstructed view of cold space. These waveguide runs had lengths of approximately one foot.

A number of problems arose during SMMR operation which made absolute calibration of the brightness temperature images difficult. An excellent review of these problems is ,given by Francis [15]. Some of the problems involved the coupling between horizontal and vertical polarization due to the antenna scan geometry - these will not affect TMR and will not be discussed here, Problems with SMMR which may also affect TMR involve the MFFH design and the hardware implementation of the hot/cold antenna calibration. The very wide bandwidth of the MFFH (6,6-37.0 GHz) necessitated compromises in its

operation at individual SMMR frequencies. For example, the flare angle of the feed horn was larger than optimal at the higher frequencies in order to accommodate the lower frequencies in a reasonable size. At the higher frequencies, this produced additional phase errors in the aperture plane of the feed, a poorer impedance match at the output ports of the feed, and a ripple in the center of the main reflector illumination pattern [K. Green, *personal communication, 1988].* The edge. taper used to illuminate the main reflector was also a compromise, between the desire for high spatial resolution and for high beam efficiency. The taper used resulted in a significant amount of spillover past the main reflector and scattering from the six rods supporting the main reflector. This degraded the beam efficiency of the antenna.

The use of microwave ferrite switches, extended runs of waveguide, and separate sky horn antennas to provide hot and cold points for the T_A calibration introduced a number of problems [14]. The actual cold point T_A measured by the radiometer had to be estimated from a radiative transfer model for propagation of the incoming cold space brightness temperature ($\approx$ 2.7 K) through the subsequent hardware. Similarly, the radiometer measurements made with the ferrite switch matrix in the MFFH viewing mode included radiative transfer effects through the MFFH, the waveguide run between the MFFH and the switch, and the switch itself. The hot point T_A measurement made while viewing a blackbody waveguide termination also included propagation through the ferrite switch, Errors in the radiative transfer model used for these effects produced errors in the T_A calibration which were sensitive to variations in the physical temperature of the microwave hardware. The model errors resulted from an incomplete cycling of the instrument physical

temperatures during the pre-flight T/V calibration procedure. The SMMR calibration hardware encountered significant variations in its physical temperature on orbit over periods of minutes due to solar heating and the calibration was degraded as a result [15], One other problem with the cold point calibration measurements for SMMR was caused by the sun entering the main beam of the sky horn [6].

B. TMR instrument modifications

TMR is a modified version of a backup SMMR flight instrument which was not used during the SeaSat or Nimbus programs. A picture of the instrument is shown in Figure 1 and a block diagram in Figure 2. A summary of the instrument engineering specifications for TMR is given in Table 1. Several of the changes made to SMMR followed naturally from the specific requirements of the T/P mission. The antenna scanning mechanism was removed since TMR is strictly a nadir-viewing instrument. The lower frequency channels (6,6 and 10.7 GHz) were removed since they are not needed to estimate wet tropospheric path delay over the ocean [16]. The polarization select switch for the 18.0 GHz channel is set permanently in the horizontal polarization position and the vertical polarization output port of the MFFH at this frequency is terminated with a matched load. Similarly, the vertical polarization radiometer channel at 37,0 GHz was removed and this MFFH port was also terminated with a matched load, leaving a single 37.0 GHz radiometer connected to the horizontal port of the MFFH. These modifications were possible because the nadir viewing geometry eliminates any significant polarization sense. (The effects of a small anisotropy which is present in the cross-wind/along-wind surface emissivit y [17] is negligible, provided all three TMR channels are polarized in the same direction.) Whereas SMMR used one radiometer at 21.0 GHz to

monitor both polarizations, TMR has two identical, independent radiometers at 21.0 GHz, one connected to each of the two polarization output ports from the MFFH. Each of these radiometers has a ferrite switch matrix assembly with the polarization select switch set permanently in the position which is connected to the MFFH. Only one of the 21,0 GHz channels will be turned on initially. The other will serve as a back up in case of failure, Only the 21,0 GHz channel is redundant because it is critical to the T/P mission. TMR path delay retrieval performance would degrade but still be useful if either of the other two, but not the 21.0 GHz, channels fails [16]. Another straightforward modification to the SMMR design involved the positioning and pointing geometry of the sky horns. A sky horn location and pointing geometry was selected which should prevent the sun from entering a cone centered on its boresight and with a half angle of 60°. This lies well outside of the nominal sky horn HPBW of 24°.

The MFFH used for SMMR is built in three sections. The top section starts at the 5.25" diameter circular aperture of the feed horn and tapers in with a ring-loaded corrugated conical horn to a circular waveguide with coaxial output ports for the 6.6 GHz channels. The next section is a circular waveguide with output ports for the 10.7 GHz channels, followed by a tapered circular-to-rectangular waveguide transition, The last section begins with output ports at 18.0 and 21.0 GHz, then tapers and transitions to a rectangular waveguide with output ports at 37.0 GHz. For TMR, the top section has been replaced by a similar ring-loaded corrugated horn with a narrower flare angle which only opens out to a circular aperture diameter of 4.0". The middle section has been replaced by a tapered circular-to-rectangular waveguide transition with no output ports. The final section has been left

unchanged. A cross sectional drawing of the TMR MFFH is shown in Figure 3.

The reduced flare angle of the TMR MFFH provides a more gradual transition at the higher frequencies from waveguide to free space propagation. This reduces the phase error at the aperture, plane, which in turn improves the feed radiation pattern and the impedance match at the MFFH output ports. A sample of the MFFH radiation pattern at 21.0 GHz before and after the modification to the flare angle is shown in Figure 4. The SMMR feed pattern has a ripple across the center which has been eliminated. The power level of the feed pattern at $\pm 41°$ corresponds to the edge illumination of the main reflector. This level has also been reduced with the TMR MFFH. The under-illumination of the main reflector will tend to increase the HPBW of the complete TMR antenna pattern and decrease its overall far sidelobe level by reducing the spillover past the reflector and the scattering off of the six reflector support rods. The main reflector used for TMR is identical to those used for SMMR. A summary of the TMR antenna performance is given in Table 2, along with a comparison to earlier SMMR performance specifications. A number of the TMR specifications are described in greater detail in Janssen *et* al. [4]. The HPBW and resulting Earth footprint have increased with TMR by approximately 5%. The beam efficiency has increased on average by 2.4%. Most significantly, the percentage of power received from the far sidelobes of the antenna which will lie off the earth during the mission has been reduced from 5.7-10.1 % to 0.4-0.7%. This will greatly improve the accuracy of the sidelobe corrections in the brightness temperature calibration algorithm [4].

Radomes were added to the TMR MFFH and sky horns to reduce short term fluctuations in the physical temperatures of these antennas caused by solar heating. These radomes are flat 3/8" thick pieces of polystyrene (styrofoam)

with a mass density of 2 lbs/ft^3. They are positioned in front of the horns, perpendicular to their central axis and wide enough to block all incident sun light. Pre-flight thermal analysis indicates that the radomes will significantly reduce the expected on orbit variations in the MFFH and sky horn temperatures. A number of tests were conducted to estimate the effects of these radomes on TMR performance.

Electrical radome performance was estimated using an available ground based water vapor radiometer (WVR) operating at 20.7 and 31.4 GHz. T_A was measured while viewing the zenith sky both with and without the radome. For the determination of insertion loss, the radome was set against a flat metal reflecting plate angled at 45° relative to both the WVR antenna boresight and zenith. This reduced the effects of reflections from the radome. For the characterization of reflections, the radome was positioned directly in front of the WVR antenna and perpendicular to its boresight. The distance between the radome and the WVR antenna was then varied to measure standing waves in T_A due to reflections from the radome. The insertion loss of the polystyrene was determined to be 0.2% $\pm$0. 1 % per inch of radome thickness at both 20.7 and 31.4 GHz. The standing wave characterization consisted of a Fourier analysis of the variation in T_A with radome position, to extract that harmonic which was due to reflections from the radome. A sample of the standing wave data is shown in Figure 5. The results of the standing wave test are summarized in Table 3, The effects of reflections are substantially less than that of general purpose polystyrene, which has a density of 15-20 lbs/ft^3 and a dielectric constant of approximately 2.6 [18]. Low density polystyrenes such as are used here have dielectric constants in the range 1,03-1.16 [19].

The effects of ultraviolet (UV) radiation on the radome material were

also tested. A sample of the radome was exposed to a 75 watt Xenon lamp producing ≈ 1,400 W/m^2 of UV radiation at the center and ≈ 300 W/m* at the edge of a 1 inch spot. The expected incident UV radiation on orbit is 118 W/m^2 with intermittent exposure by the sky horn radome during approximately 12% of the mission and at grazing angles of 60° or greater. The MFFH radome will be exposed during approximately 4 % of the mission and at grazing angles of 42° or greater. The polystyrene sample was exposed for a total of 2.7 times the mission exposure level for the sky horn radome (7.8 times the MFFH radome exposure). The 1 inch spot discolored almost immediately, from an initial white to a yellowish-brown color, No further changes were observed. Subsequent to the exposure, a microscopic examination found that the discoloration extended approximately 0.0015" into the material, uniformly across the 1 inch spot. This indicates that the discoloration is a self-limiting process. Additionally, an RF transmission test after exposure found no significant change and a study of the impact of discoloration on the radome thermal balance was satisfactory.

C. *TMR Instrument Calibration*

TMR calibration can be divided into three stages. The first stage is T_A calibration. Raw digital counts are recorded by TMR with the ferrite switch matrix at the input to the radiometer electronics directed to each of the matched load termination (hot point), sky horn (cold point), and MFFH (intermediate earth viewing data point) source positions. The operational sequence of data taking is fourteen 1 s earth observations, followed by a single 1 s hot point measurement, then another fourteen 1 s earth observations, then a single 1 s cold point measurement. These digital counts are converted to the equivalent temperature which would be measured if the

entire TMR instrument were enclosed in a uniform blackbody environment. This T_A calibration algorithm is described in detail in the following section, RMS errors due to stochastic radiometer noise (AT) are approximately 0.27 K at each frequency channel. The precision of the radiative transfer model for the losses and reflections in the calibration hardware is estimated to be approximately 0,38-0.40 K at all channels. Possible biases in the radiative transfer model will be corrected after launch. The expected accuracy of T_A with this correction is 0.54-0.57 K.

The second stage of TMR calibration deconvolves the effects of the antenna pattern to estimate the brightness temperature of the earth in the direction of the TMR antenna main beam, This brightness temperature calibration algorithm is discussed in detail by Janssen *et al.* [4]. In summary, detailed measurements of the antenna pattern were made before aunch. Estimates of the contribution to T_A from radiation entering the on-earth sidelobes of the antenna were then made by modeling the mean brightness temperature of the Earth as seen by TMR at off nadir angles, Similarly, the contribution to T_A from far sidelobes viewing cold space was modeled. These contributions were subtracted from the measured T_A. Finally, a gain correction was made to account for the reduced sensitivity of the main beam of the antenna due to the integrated sensitivity of the sidelobes. The RMS error expected with this algorithm is 0.71-0.77 *K,* This includes the expected error in T_A. These brightness temperature calibration errors are equivalent to a 0.69 cm error in path delay [16]. In addition, the errors due to differences in antenna footprint size between the TMR channels, and between TMR and the altimeter footprint, must be considered. The. RMS decorrelation of the spatially averaged path delays for the various footprint sizes amounts to an

additional error in path delay of 0.32 cm [4],

The final stage of TMR calibration involves the wet tropospheric path delay retrieval algorithm which estimates vertical path delay from the nadir brightness temperatures. This retrieval algorithm is described in detail by Keihm *et al.* [16]. In summary, the intrinsic residual RMS error in the path delay retrieval is estimated to be 0.37 cm. This error is due to the inexact correlation between brightness temperature and path delay. In addition to this source of error, uncertainties in the models used for water vapor, oxygen and liquid water absorption, as well as those used for the sea surface flux, increase the total retrieval error to 0.93 cm, When combined with the 0.69 cm error due to brightness temperature calibration and the 0.32 cm error due to spatial decorrelation, this results in a total TMR retrieval error of 1.20 cm.

111. ANTENNA TEMPERATURE CALIBRATION

A. Derivation of the hardware radiative transfer model

The TMR front-end ferrite switch assemblies allow for three different input sources: the Earth viewing antenna, the cold sky viewing calibration horn, and the hot load at instrument ambient temperature. The system temperature detected by the TMR back-end in each of these cases is determined by the radiative transfer of the signal from its input source to the output of the ferrite switch assembly.

The model used for the signal flow from the Earth viewing antenna input source is shown in Figure 6. In the figure, α_f, α_w, and α_s are the numeric power transmission coefficients through the antenna feed, the waveguide from the feed to the ferrite switch, and the ferrite switch assembly, respectively. T_f, T_w, and T_1 are the physical temperatures of these same components (in

units of degrees K), and Γ_f and Γ_s are the numeric power reflection coefficients at the feed and ferrite switch, respectively,

Beginning at the feed, a signal incident on the antenna with brightness temperature T_A will reach the output of the switch and isolator attenuated to a brightness temperature of

$$T_A(1 - \Gamma_f)\alpha_f\alpha_w(1 - \Gamma_s)\alpha_s \quad (1)$$

Since the impedance mismatches are not very large, all multiple reflections will be neglected. The thermal self-emission from the feed itself has a direct and a reflected path to the output. If the relative phase length between these two paths is denoted by ϕ_f, then the contribution to the output by the feed is

$$T_f(1 - \alpha_f)(1 - \Gamma_s)\alpha_w\alpha_s \mid 1 + (\Gamma_f\alpha_f)^{1/2}e^{j\phi_f} \mid^2 \quad (2)$$

Note, however, that the feed losses are distributed over the length of the component, not lumped at a single point. Each differential part of the loss will have its own relative phase length associated with it. If the component is an appreciable number of half-wavelengths long, then these phase lengths will tend to average out. There will be no net constructive or destructive interference between the direct and the reflected emission from the feed to the output. In this case, the power in the two contributions can be added directly. Tbe contribution to the output by tbe feed is, then

$$T_f(1 - \alpha_f)(1 - \Gamma_s)\alpha_w\alpha_s(1 + \Gamma_f\alpha_f) \quad (3)$$

Similarly, the thermal emission by the waveguide will add in power from the direct and reflected paths, This contribution to the output is

$$T_w(1 - \alpha_w)(1 - \Gamma_s)\alpha_s(1 + \Gamma_f\alpha_f^2\alpha_w) \quad (4)$$

The thermal emission by the switch and isolator has three paths to the output . The direct path is

$$T_I(1 - \alpha_s) \tag{5}$$

where T_I, the "instrument" temperature, is the temperature of the large ferrite switch assembly which includes the Dicke and hot calibration loads. The brightness temperature of the thermal emission leaving the switch and isolator toward the antenna is equal to its physical temperature, The component of this emission which reflects off the switch mismatch back into the switch reaches the output as

$$T_I \Gamma_s \alpha_s \tag{6}$$

The component which reflects off the feed mismatch reaches the output as

$$T_I(1 - \Gamma_s)^2 \Gamma_f \alpha_f^2 \alpha_w^2 \alpha_s \tag{7}$$

The phase relationship between the emission described by (5) and by either of (6) and (7) will probably average out as above due to the physical size of the switch and isolator assembly. However, there is an exact phase relationship between the emission described by (6) and (7) since they can both be referenced to a single plane, namely the input port of the switch assembly. Let ϕ describe their relative phase upon arriving at the output. Then their contribution is

$$T_I \alpha_s \left| \Gamma_s^{1/2} + (1 - \Gamma_s) \Gamma_f^{1/2} \alpha_f \alpha_w e^{j\phi} \right|^2 \tag{8}$$

Let T_A' denote the total thermal emission leaving the output port of the front end. It will consist of the sum of (l), (3), (4), (5), and (8), or

$$
\begin{aligned}
T'_A = {} & T_A(1-\Gamma_f)(1-\Gamma_s)\alpha_f\alpha_w\alpha_s \\
& + T_f(1-\alpha_f)(1-\Gamma_s)\alpha_w\alpha_s(1+\Gamma_f\alpha_f) \\
& + T_w(1-\alpha_w)(1-\Gamma_s)\alpha_s(1+\Gamma_f\alpha_f^2\alpha_w) \\
& + T_I\left[(1-\alpha_s) + \alpha_s|\Gamma_s^{1/2} + (1-\Gamma_s)\Gamma_f^{1/2}\alpha_f\alpha_w e^{j\phi_2}\right]
\end{aligned} \tag{9}
$$

The model used for the signal flow from the calibration horn is the same and the resulting equation of radiative transfer is similar to that derived above, except that α_h, $\alpha_{h\text{-}w}$ and $\alpha_{h\text{-}s}$ are the corresponding transmission coefficients along the calibration path, T_h and $T_{h\text{-}w}$ are the temperatures of the calibration horn and connecting waveguide, respectively, and Γ_h are $\Gamma_{h\text{-}s}$ are the reflection coefficients at the horn and ferrite switch. If T_c' is the total thermal emission leaving the output port of the ferrite switch assembly and $T_c \approx 2.7$ K is the input source to the calibration horn, then

$$
\begin{aligned}
T'_c = {} & T_c(1-\Gamma_h)(1-\Gamma_{h\text{-}s})\alpha_h\alpha_{h\text{-}w}\alpha_{h\text{-}s} \\
& + T_h(1-\alpha_h)(1-\Gamma_{h\text{-}s})\alpha_{h\text{-}w}\alpha_{h\text{-}s}(1+\Gamma_h\alpha_h) \\
& + T_{h\text{-}w}(1-\alpha_{h\text{-}w})(1-\Gamma_{h\text{-}s})\alpha_{h\text{-}s}(1+\Gamma_h\alpha_h^2\alpha_{h\text{-}w}) \\
& + T_I\left[(1-\alpha_{h\text{-}s}) + \alpha_{h\text{-}s}|\Gamma_{h\text{-}s}^{1/2} + (1-\Gamma_{h\text{-}s})\Gamma_h^{1/2}\alpha_h\alpha_{h\text{-}s}e^{j\phi_h}|^2\right]
\end{aligned} \tag{10}
$$

where ϕ_h is twice the relative electrical phase separation between the horn and the ferrite switch input port. The exact value used for the cosmic background brightness temperature, T_C, varies with frequency due to the strict proportionality assumed between brightness temperature and radiated power. While the physical temperature of the cosmic background radiation is 2.735 K, independent of frequency, the equivalent brightness temperature varies due to a frequency dependent departure of the full **Planck blackbody** radiation expression from the **Rayleigh-Jeans** approximation. This departure is

approximately constant over the range of expected brightness temperatures viewed by the TMR main reflector. However, the full Planck correction is different near the 2.7 K scene viewed by the cold sky horn, This difference in the correction is accounted for by adjusting T_C. This forces a constant Planck correction at all scene brightness temperatures and allows the TMR gain to be computed correctly from the hot and cold digital counts.

The signal flow from the hot load is given by

$$T_H' = T_I \tag{11}$$

where T_H' is the output of the ferrite switch. This follows since the hot load is connected directly to the switch and both are at physical temperature T_I.

The TMR is a Dicke Radiometer which is sensitive to the difference between the thermal emission from an input source and from an ambient load. Digital measurements C_N (N = A, C, or H) are made for the three input sources (Antenna, Cold sky, or Hot load). These measurements are related to the output thermal emission derived above by

$$C_N = G(T_N - T_I) + C_0 \tag{12}$$

where N = A, C, or H, G is the gain of the radiometer in units of digital counts/degree, and Co is a possible offset.

The offset, Co, is found from the hot measurement, C_H. Substituting (11) into (12) gives:

$$CO = C_H \tag{13}$$

The gain, G, is found from the cold sky measurement, Cc. Combining (12) and (13) for the case N = C gives

$$G = \frac{C_H - C_C}{T_I - T_C'} \tag{14}$$

The thermal emission, T_A', is found by combining (12), (13), and (14) for the case N == A, giving

$$T_A' = \frac{(C_A - C_H)(T_I - T_C')}{(C_H - C_C)} + T_I \tag{15}$$

The antenna temperature, TAO, is found by inverting (9) with respect to the measurement of T_A' described by (15). This results in an estimate of the antenna temperature described by

$$T_{AC} = \frac{C_A - C_H}{C_H - C_C}\left[a_1 T_c + a_2 T_h + a_3 T_{h-w} + a_4 T_I + a_5 T_f + a_w T_w + a_6 T_I\right] \tag{16}$$

where

$$a_1 = -(1 - \Gamma_h)(1 - \Gamma_{h-s})\alpha_h \alpha_{h-w} \alpha_{h-s} / D$$

$$a_2 = -(1 - \alpha_h)(1 - \Gamma_{h-s})\alpha_{h-w}\alpha_{h-s}(1 + \Gamma_h \alpha_h) / D$$

$$a_3 = -\left[(1 - \alpha_{h-w})(1 - \Gamma_{h-s})\alpha_{h-s}(1 + \Gamma_h \alpha_h^2 \alpha_{h-w})\right] / D$$

$$a_4 = \left\{1 - \left[(1-\alpha_{h-s}) + \alpha_{h-s} \left| \Gamma_{h-s}^{1/2} + (1 - \Gamma_{h-s})\Gamma_h^{1/2}\alpha_h \alpha_{h-w} e^{j\phi_h}\right|^2\right]\right\} / D$$

$$a_5 = -\left[(1 - \alpha_f)(1 - \Gamma_s)\alpha_w \alpha_s (1 + \Gamma_f \alpha_f)\right] / D$$

$$a_w = -\left[(1 - \alpha_w)(1 - \Gamma_s)\alpha_s (1 + \Gamma_f \alpha_f^2 \alpha_w)\right] / D$$

$$a_6 = \left\{1 - \left[(1-\alpha_s) + \alpha_s \left| \Gamma_s^{1/2} + (1 - \Gamma_s)\Gamma_t^{1/2}\alpha_f \alpha_w e^{j\phi}\right|^2\right]\right\} / D$$

and

$$D = (1 - \Gamma_f)(1 - \Gamma_s)\alpha_f\alpha_w\alpha_s$$

In practice, the thermal emission from the waveguide between the MFFH and the ferrite switch assembly is negligible, and a_w is taken to be zero, The remaining calibration coefficients, a_1 - a_6, have been estimated from data measured during T/V testing of TMR.

Equation (12) assumes a purely linear relationship between the digital outputs (voltages) and temperature inputs (powers), Actual microwave radiometers exhibit a small non-linearity, typically due to amplifier compression and/or non-"square-law" detector behavior. Analysis of the measurements made during T/V testing is discussed below, The analysis suggests the form of the non-linearity correction which should be used. This second order effect is well modeled by a quadratic term which is centered about a non-zero T_A. In addition, the degree of non-linearity is strongly correlated with the instrument temperature. Since the non-linearity at all temperatures is small, a linear dependence on instrument temperature is sufficient to model this correlation. The quadratic correction to T_A is given by

$$T_A = T_{A0} + a_7(T_{A0} - a_8)^2 + a_9 \quad (17)$$

where

T_A is the final, fully calibrated antenna temperature

TAO is given by (16)

and where

$$a_i = b_{i1}T_I + b_{i2} \text{ for } i = 7, 8, \text{ and } 9 \quad (18)$$

where

b_{ij} are constants derived from the T/V test data

T_I is the TMR instrument temperature

B. Thermal/Vacuum antenna temperature calibration/validation

1. Overview of thermal/vacuum test

The T/V test consists of a series of calibration runs with the TMR operating at different physical temperatures, Temperature controlled black body targets are positioned in front of both the MFFH and the sky horns, These targets are also run at different temperatures, A calibration run consists of a set of digital counts recorded while the radiometer is switched to look at each of the MFFH target, the sky horn target, and an internal ambient matched load.

Physical temperature variations are controlled differently for different parts of the hardware, The targets are controlled by LN_2 and gaseous N_2 manifolds soldered to the back sides of the heatsinks surrounding the absorbing material. The overall instrument temperature is controlled by similarly heated and cooled jackets attached to the sides of the instrument, where the passive radiant coolers are normally attached in flight. The temperatures of individual parts of the microwave front-end electronics are independently controlled by small electric heater strips. There are fourteen of these heaters, located as follows: 1 & 2) around the outside of the upper MFFH; 3) around the throat of the MFFH; 4) midway along the 18 GHz waveguide run between the MFFH and the instrument ferrite switch assembly; 5, 6, & 7) same as 4 for the 21 H, 21 V, and 37 GHz channels, respectively; 8) around the outside of the single cal horn shared by the 18 and 21H GHz channels; 9 & 10) same as 8 for the 21V and 37 GHz channels, respectively; 11) midway along the waveguide run between the cal horn for the 18 GHz channel and the instrument

ferrite switch assembly; and 12, 13, & 14) same as 11 for the 21H, 21V, and 37 GHz channels, respectively.

Temperature variations can be divided into three parts, In the first part, the instrument temperature, T_I, is varied from 5° C to 50° C, in steps of 5° or 10" C, by controlling the large temperature jackets attached to the sides of the instrument. At each plateau, the MFFH target temperature is varied from 100K to 350K in 35K steps and the sky horn target temperature is maintained at ≈ 80K. This sequence is illustrated in Figure 7. No independent control is maintained of the individual heater strips; they arc always off and the assemblies they are attached to typically had monotonic gradients running from the instrument temperature to the target temperature. At each instrument and target temperature, a calibration run was made after the temperature had stabilized.

The second part of the temperature variation procedure occurred at each instrument plateau and at a fixed MFFH target temperature of either 100K or 240K. The individual heater strips were turned on in the following sequence: 1) MFFH and MFFH waveguide heaters (#1-7) turned on with temperature set point 10K higher than the overall instrument temperature; 2) Heaters #l-7 turned off and heaters #11-14 (waveguides between sky horn and instrument) turned on with a temperature set point also 10K above the instrument; and 3) Heaters #11-14 turned off and heaters #8- 10 (sky horn) turned on with a set point 10K above the instrument. The effect which these heater adjustments had on the physical temperatures of the microwave components is shown in Figure 8, which plots actual temperatures recorded during the test, A calibration run was performed before step 1 and and after each of steps 1-3. These independent variations in component temperatures allowed the effects of thermal emission from the

components to be isolated and quantified.

The third part of the test consisted of a set of calibration measurements made while the cold sky horn target temperature was maintained at 296K. Instrument and MFFH target temperatures were also at ambient temperature during this time.

2. T/V data reduction and analysis

T/V data reduction can be divided into three segments: 1) the calibration coefficients related to thermal emission from and attenuation by the MFFH, cold sky horn, waveguide to the cold sky horn, and Dicke and calibration ferrite switch assemblies (a_2-a_6) are estimated by multi-linear regression of data taken when their temperatures were varied in a linearly independent manner; 2) the calibration coefficient relating to the dependence of T_A on the cold sky horn target temperature (al) is estimated by linear regression of data taken when the cold sky horn target was at ambient, combined with an equal quantity of data selected from the large database with the target at 80K; and 3) the calibration coefficients relating quadratic correction terms to the instrument temperature (b_{71}-b_{92}) are estimated by linear regression of the best fit quadratic corrections at each instrument temperature. Step 1 requires an estimate of the result of step 2. Likewise, step 2 requires that the coefficients from step 1 are known. Irk practice, these steps are iterated until the coefficient estimates converge. Step 3 is then evaluated using these coefficients.

2.1, Multi-linear estimate of hardware emission

Equation (16) can be rewritten for the case of N different configurations of the instrument and MFFH target physical temperatures in the form

$$\vec{x} = \mathcal{J}\vec{y} \tag{19}$$

where

$$x_i = T_{Ai} - a_1 D_i T_C, \; i = 1..N$$

$$D_i = \frac{C_{Ai} - C_{Hi}}{C_{Hi} - C_i}, \; i = 1..N$$

T_{Ai} is the physical temperature of the MFFH target, i = 1, .N

T_C is the physical temperature of the sky horn target

$\vec{y}$ is the vector of coefficients to be estimated, a_2 through a_6

$\mathcal{J}$ is an N x 5 matrix given by:

$$\mathcal{J} = \begin{bmatrix} T_{h1} & D_1 T_{h\text{-}w1} & T_{i1} & T_{f1} & T_{i1} \\ T_{h2} & D_2 T_{h\text{-}w2} & T_{i2} & T_{f2} & T_{i2} \\ \vdots & \vdots & \vdots & \vdots & \vdots \\ D_N T_{hN} & D_N T_{h\text{-}wN} & D_N T_{iN} & T_{fN} & T_{iN} \end{bmatrix} \tag{20}$$

The vector of coefficients, $\vec{y}$, is estimated from the data by minimum squared error inversion of (19)

$$\vec{y} = (\mathcal{J}^t \mathcal{J})^{-1} \mathcal{J}^t \vec{x} \tag{21}$$

where t denotes the matrix transpose operation.

A numerical simulation was performed to determine the ability of this T/V test to accurately retrieve the calibration coefficients. This simulation used approximate values for the coefficients, based on SMMR data, to estimate the T/V data. It then evaluated the performance of the multi-linear regression in a number of ways. It was found that the actual error in the coefficient estimates was highly correlated with the root-sum-square of the main diagonal of the covariance matrix describing the multi-linear estimator.

This RSS covariance specifically computes the error in a particular coefficient per degree K error in the estimate of true antenna temperature, as determined by the physical temperature of the MFFH target. The MFFH target temperature was measured by a network of 8 precision platinum temperature sensors (accuracy 0.05K) imbedded in the iron loaded epoxy absorbing material. T_A estimates from these measurements should be accurate to better than 0.5 K.

Preliminary analysis of the T/V data revealed a strong coupling between the coefficients a_2 and a_3. These coefficients account for thermal emission by the sky horn and its connecting waveguide. This coupling was indicated by an unacceptably high covariance (> 100%), and may be due to either a strong temperature coupling, a relatively low insertion loss for one of the two components, or both. This coupling was eliminated by substituting a single unknown coefficient for the two in the multi-linear regression and using the average physical temperature of the two components. (The coefficients reported below for a_2 and a_3 are each half the retrieved coefficient.) The retrieved coefficients and RSS covariance estimates of coefficient accuracy for each TMR channel are given in Table 4.

2,2, Linear estimate of cold sky temperature sensitivity

Calibration runs were made with the sky horn target temperature at both 80K and ambient. This is especially important for this particular parameter because the cold space temperature seen by the horn in flight will be significantly different (≈ 2.7 K), which implies a significant extrapolation of the pre-flight conditions.

Equation (16) can be rewritten, to regress against coefficient al, as:

$$T_A - D[a_2 T_h + a_3 T_{h-w} + a_4 T_{i-1} - a_5 T_h - a_6 T_i] = a_1 D T_c + b \qquad (22)$$

where

$$D = -\frac{C_A - C_H}{C_H - C_C}$$

and b is a possible offset term. The coefficients a_1 estimated for each TMR channel from this regression are given in Table 4.

2,3. Temperature dependent non-linear correction

Using (16) and calibration coefficients a_1-a_6, T_A can be estimated from the digital counts for each calibration run and compared with the "true" antenna temperature as determined by the temperature of the MFFH target. Figure 9 plots this comparison for the 18 GHz TMR channel, with instrument temperature as a parameter. These calibration runs were made without special temperature gradients induced by the electric heater strips. They are independent tests of the accuracy of the coefficients, which were estimated from the set of calibration runs made with the heater strips on. The error between the true and estimated antenna temperatures is plotted vs. the true antenna temperature to illustrate the non-linear behavior of the electronics. At each instrument temperature, a quadratic curve can be seen. The magnitude of the curvature, the base of the parabola, and its vertical offset all vary with instrument temperature, One possible mechanism for this behavior is the temperature dependence of amplifier gain. Gain typically increases with decreasing temperature. Higher gain would increase the power level incident on the detector diode, driving it further from its optimal, linear power region. The quadratic curvature is seen in the figure to be larger at lower

temperatures, confirming this behavior, Another possible cause of the observed non-linearity is the RF leakage between ports of the calibration ferrite switch. Leakage will add a small fraction of T_A onto the measurement of T_H, which results in a T_A dependent gain and offset. Both sources of non-linearity are consistent with the behavior observed during T/V testing, and the correction described below should remedy either one.

Data analysis consisted of minimizing the error between the estimated and true antenna temperatures by adjusting the curvature, offset, and base of the quadratic component of error and then adding this to the estimated antenna temperature. This is the correction described by (17). Because the non-linearity was temperature dependent, the optimal quadratic coefficients were determined independently at each instrument temperature. An example of the temperature dependent nature of the correction terms for the 18 GHz channel is shown in Figure 10. While the dependence on temperature. doesn't appear to be linear, it is monotonic and, since the quadratic correction is small (typically $\leq$ 0.1 K in each channel), a linear model will suffice.

Linear fits of each of the quadratic correction terms to instrument temperature were performed for all TMR channels. The resulting calibration coefficients are given in Table 4.

C. *Antenna temperature calibration error analysis*

The residual error in the fully calibrated antenna temperature is plotted in Figures 11a-c for the three TMR channels. These plots only include MFFH target temperatures and instrument temperatures which are predicted by thermal analysis to be encountered in flight; the 350 K target temperature and 277 K instrument temperature data have been removed. Likewise, the RMS residual errors quoted in the figures also exclude these data. The RMS residuals are

0,24, 0.24, and 0.19 K at 18, 21, and 37 GHz, respectively. Comparison of Figure 11A with Figure 10 shows that systematic instrument temperature dependent and T_A dependent effects have been largely removed by the non-linearity correction. The RMS residual has also been lowered, by 0.98, 0.59, and 0.55 K in an RSS sense, at 18, 21, and 37 GHz, respectively. These values can be thought of as the degree of non-linearity present in the TMR system transfer function.

The precision of the T_A calibration in flight due to measurement noise is found from an RSS combination of the individual error terms in (16). The small contribution from the quadratic correction term can be neglected. If ΔT_A is the RMS precision in the estimate of T_A, then

$$\Delta T_A^2 = \Delta T^2 + AC^2 \left[\left(\frac{\partial T_A}{\partial C_A} \right)^2 + \left(\frac{\partial T_A}{\partial C_H} \right)^2 + \left(\frac{\partial T_A}{\partial C_C} \right)^2 \right] \quad (23)$$

$$+ \Delta T_c^2 \left(\frac{\partial T_A}{\partial T_C} \right)^2$$

$$+ \Delta T_n^2 \left| \left[\frac{\partial T_A}{\partial T_h} 1 \right]^2 + \left(\frac{\partial T_A}{\partial T_{h-w}} \right)^2 + \left(\frac{\partial T_A}{\partial T_I} \right)^2 + \left(\frac{\partial T_A}{\partial T_f} \right)^2 \right|$$

where $AT \approx 0.27$ K is the radiometer noise floor, $AC = 1/2$ count is the quantization error, ΔT_C is the uncertainty in the cosmic background brightness temperature, and $A T_n = 0.05$ K is the measurement accuracy of the platinum temperature sensors, The first term *(AT)* is found to dominate the others, and the total RSS error is $A T_A \approx 0.32$ K, The net precision of the T_A calibration is an RSS combination of the $A T_A$ measurement precision with the model accuracy of the T_A calibration algorithm, as determined by the T/V test residuals at the four TMR frequencies, This results in a 0,38-0.40 K residual error. The

errors associated with antenna temperature calibration are summarized in Table 5.

The 0.4 K RSS T_A residuals should be thought of as measures of repeatability and precision in the T_A retrieval algorithm. The residuals measure the ability of the TMR data system to track changes in the MFFH target temperature. Systematic offsets between the MFFH target temperature and the true antenna temperature will not be corrected. Possible sources of these systematic include: 1) differences between the arithmetic average of the temperatures of the 8 thermistors distributed across the MFFH target and the MFFH beam-averaged temperature actually sensed by the TMR; 2) Local and/or global deviations of the "black body" target's emissivity from unity; and 3) MFFH far sidelobe and backlobe contributions to the true antenna temperature. These error sources are all probably small, but are also all probably on the same order as the final RMS residuals quoted here, and should, therefore, not be ignored, We conservatively estimate these additional errors to be equal in magnitude to the residual T/V errors, resulting in a RSS total T_A error of 0,54 -0.57K for the three TMR channels.

A final correction to the TMR calibration is planned after launch which will nominally adjust each channel by a constant offset [16]. This correction will be based on coincident measurements of the downwelling brightness temperature from the atmosphere made by upward looking WVRs during T/P overpasses of island sites. Correlations between WVR and TMR measurements will allow the differences between TMR brightness temperatures to be predicted with high accuracy. Comparisons between WVR and TMR wet tropospheric path delay estimates can then be used to establish an absolute TMR calibration. This calibration will, in part, correct for the systematic present in the T_A

calibration algorithm. Other possible systematic offsets, e.g. in the brightness temperature calibration algorithm [4], will also be corrected at this time. The post-launch calibration effort is estimated to result in path delay retrievals which are accurate to 1.20 cm. This corresponds to a brightness temperature accuracy of 0.71-0.7”1 K and a T_A accuracy of 0.54-0.57 K.

ACKNOWLEDGMENTS

The authors wish to acknowledge the assistance of Keith Warfield of the Jet Propulsion Laboratory with the performance and analysis of the radome material UV tests. This work presents the results of one phase of research conducted at the Jet Propulsion Laboratory, California Institute of Technology, Pasadena, CA, under contract to the National Aeronautics and Space Administration.

REFERENCES

[1] G, Carlisle, A. DiCicco, H.M. Harris, A. Salama, and M. Vincent, *TOPEX/POSEIDON Project Mission Plan,* Jet Propulsion Laboratory, Pasadena, CA, Documentation number D-6862, Rev, B, 1991.

[2] C. M. Rush, *Ionospheric radio propagation models and predictions - a mini-review,* IEEE Trans. Antennas and Propag., AP-34, 1163-1170, 1986.

[3] J. Saastamoinen, *Atmospheric correction for the troposphere and stratosphere in radio ranging of satellites,* Geophysical Monograph #15, AGU, Washington, D. C., William Byrd Press, Richmond, VOA, 1972.

[4] M .A. Janssen, C.S. Ruf, and S.J. Keihm, *TOPEX/POSEIDON Microwave Radiometer (TMR): 2, Antenna pattern correction and brightness temperature algorithm,* this issue, pp. iiii-jjjj, 1993.

[5] B.D. Tapley, J.B. Lundberg, and G.H. Born, *The SeaSat altimeter wet tropospheric range correction,* J. Geophys. Res., 87, 3213-3220, 1982,

[6] E.G. Njoku, J.M. Stacey, and F.T. Barath, *The SeaSat Scanning Multichannel Microwave Radiometer (SMMR): Instrument description and performance,* IEEE J. Ocean. Engin., OE-5, 2, 100-115, 1980.

[7] D. Prabhakara, H.D. Chang, and A.T.C. Chang, *Remote sensing of precipitable water over" the oceans from Nimbus 7 microwave measurements,* J. Appl. Meteorol., 21, 59-68, 1982.

[8] R. Stewart, L.-L. Fu, and M. Lefebvre, *Science opportunities from the TOPEX/Poseidon mission,* Rep. 86-18, Jet Propul. Lab.., Pasadena, Calif., 1986.

[9] D, F, Zimbelman and A.J, Busalacchi, *The wet tropospheric range correction: Product intercomparisons* and *the simulated effect for tropical* Pacific altimeter retrievals, J. Geophys. Res., 9S, C3,

2899-2922, 1990,

[10] D, Jourdan, C. Boissier, A. Braun, and J.F. Minster, *Influence of wet tropospheric correction on mesoscale dynamic topography as derived from satellite altimetry,* J. Geophys. Res., 95, C1O, 17,993-18,004, 1990.

[11] ERS-DC Project Office, *Along Track Scanning Radiometer and Microwave Sounder,* Ref. No. DC-HO-PST-SY-008, Farnborough, Hants, UK, 1987.

[12] E.G. Njoku, E.J. Christensen, and R. E, Cofield, The *SeaSat Scanning Multichannel Microwave Radiometer (SMMR): Antenna pattern corrections - development and implementation,* IEEE J. Ocean. Engin., *OE-5, 2, 125-137, 1980.*

[13] P.N. Swanson and A.L. Riley, The *SeaSat Scanning Multichannel Microwave Radiometer (SMMR): Radiometric calibration algorithm development and performance,* IEEE J. Ocean. Engin., OE-5, 2, 116-124, 1980.

[14] A.S. Milman and T.T. Wilheit, *Sea surface temperature from the Scanning Multichannel Microwave Radiometer on Nimbus 7,* J. Geophys. Res., 90, C6, 11, 631-11, 641, 1985.

[15] E.A. Francis, *Calibration of the Nimbus 7 SMMR,* M.S. *Thesis,* Dept. of Oceanography, Oregon State Univ., Corvalis, OR, 248 pp., 1987.

[16] S.J. Keihm, M.A. Janssen, and C.S. Ruf, *TOPEX/POSEIDON Microwave Radiometer (TMR): 3. Wet troposphere range correction algorithm and pre-launch error budget,* this issue, pp. kkkk-llll, 1993.

[17] F.J. Wentz, *Measurements of Oceanic Wind Vector Using Satellite Microwave Radiometers,* IEEE Trans. Geosci. Remote Sens., vol. 30, pp. 960-972, *1992.*

[18] J.R. Birch, J.D. Dromey, and J. Lesurf, *The optical constants of some common low-loss polymers between 4 and 40 cm-l,* Infrared Physics, Vol.

21, pp. 225-228, 1981.

[19] Emerson & Cuming, *EccoFoam® PP*, Technical Bulletin, 6-2-4B, Rev. 8/76, USA, 1976.

TABLE 1. TMR Engineering Specifications

FREQUENCY (GHz)	18	21H	21V	3'7
HPBW (deg)	1.86	1.56	1.59	0.98
Beam Efficiency (%)	91.1	89.3	87.4	90.5
Predetection Bandwidth (MHz)	100	100	100	100
Integration Time (s)	1.0	1.0	1,0	1.0
Radiometer Noise, ΔT (K)	0,26	0.27	0.27	0.27
Calibrated T_B Accuracy (K)	0.77	0,74	0.79	0.71

TABLE 2. TMR Antenna Performance (and comparison with SMMR)

	TMR	SMMR
MFFH Performance		
Return Loss at output ports (dB)		
18.0 GHz	28	21
21.0 GHz, H-pol	>40	16
21.0 GHz, V-pol	23	17
37.0 GHz	32	23
Reflector edge illumination (dB)		
18.0 GHz	-24	-23
21.0 GHz, H-pol	-23	-21
21.0 GHz, V-pol	-23	-21
37.0 GHz	-29	-26
Reflector Performance		
Half Power Beam Width (deg)		
18.0 GHz	*1.86*	*1,81*
21.0 GHz, H-pol	*1.56*	*1.49*
21.0 GHz, V-pol	1.59	1.50
37.0 GHz	*0.98*	0.93
Beam efficiency[1] (%)		
18.0 GHz	91,1	88.7
21.0 GHz, H-pol	89.3	85.8
21.0 GHz, V-pol	87.4	84.2
37.0 GHz	90.5	*90.0*
Integrated on-earth far sidelobe level[2] (%)		
18,0 GHz	2.78	≈ 1.8[3]
21.0 GHz, H-pol	2.47	≈ 2.4[3]
21.0 GHz, V-pol	3.16	≈ 2.7[3]
37.0 GHz	2.15	≈ 1.5[3]
Integrated off-earth sidelobe level[4] (%)		
18.0 GHz	0,49	≈ 6.8[3]
21.0 GHz, H-pol	0.29	≈ 9.0[3]
21.0 GHz, V-pol	0.30	≈ 10.1[3]
37.0 GHz	0,37	- 5.7[3]

NOTES:
1. Percentage of power received inside 2.5 x HPBW
2. Percentage of power received between 10° and 55° off boresight
3. Estimated from measured SMMR beam efficiencies and model fit to SMMR antenna patterns
4. Percentage of power received outside 55" off boresight

TABLE 3. TMR **Radome** Standing Wave Test Results

Thickness (in)	freq **(GHz)**	T-a pk-to-pk $(K)_1$	T-sky (K) w/o **RADOME**$_2$	**w/** RADOME$_3$
1/4	20.7	0.07	19.6	19.7
	31.4	0.15	14.7	15,2
3/8	20.7	0.09	19.9	20.1
	31.4	0.07	15.2	15.9
1/2	20,7	0.11	19,9	20.4
	31.4	0.20	15.4	16.1
5/8	20.7	0,25	20.0	20.3
	31,4	0,35	15,6	16.1

(All results are for a flat sheet of **polystyrene**, 2 **lbs/ft**^{3} density.)

NOTES: 1. Fourier component of antenna temperature **corresponding** to half wavelength standing waves due to **radome** reflection

2. Zenith viewing antenna temperature without **radome**

3, The mean antenna temperature viewing the zenith sky through the **radome** averaged over the standing waves

Table 4. TMR Antenna Temperature Loss Coefficients

	TMR Frequency (GHz) 18	21H	21V	37
		Sky horn target coefficients		
a_1	-1,06502	-1.051537	-1.166330	-0.967654
		Component losses and reflections (+/- covariance errors)		
a_2	-0.111 * 5%	-0.037 * 20%	-0.038 * 11%	-0.051 ± 10%
a_3	-0.111 * 5%	-0.037 * 20%	-0.038 ± 11%	-0.051 ± 10%
a_4	1.290 * 2%	1.121 * 3%	1.251 ± 3%	1.065 * 2%
as	-0.280 * 7%	-0.176 ± 13%	-0.101 ± 24%	-00134 ± 10%
a_6	1.273 ± 2%	1.168 * 2%	1.095 ± 2%	1.126 ± 2%
		Temperature dependent quadratic correction coefficients		
b_{71}	-2.9E-06	-2.6E-06	0.0E-06	-2.4E-06
b_{72}	0.000966	0.000855	0,000226	0.000812
b_{81}	2.75524	0	0	0
b_{82}	-656.37	148.96	207.71	163.10
b_{91}	0.06504	0	0	0.018974
b_{92}	-20.63	-0,62	-1,40	-6.31
		Equivalent cosmic background brightness temperature (K)		
T_c	2.757	2.765	2.765	2.829

(NOTE: Covariance accuracy of coefficients assumes T_A accuracy of 0.5K)

(NOTE: A zero indicates marginal instrument temperature dependence)

Table 5. Antenna Temperature Calibration Error Budget

(All values in units of K)

	TMR Frequency (GHz) 18	21H	21V	37
Stochastic Noise	0.26	0,27	0.27	0.27
Digitization, Temp. Sensor error, and T_C error	0.18	0.18	0.18	0,18
T_A model residual	0.24	0.24	0.19	0.19
RSS T_A Precision	0.40	0.40	0.38	0,38
In-flight T_A Bias	0.40	0.40	0.38	0.38
RSS T_A Accuracy	0.57	0.57	0.54	0.54

FIGURES CAPTIONS

Figure 1. The TMR Instrument

Figure 2. TMR Functional Block Diagrams. (A) System design and (B) Typical radiometer channel.

Figure 3. TMR Multi-frequency Feed Horn (MFFH) (note: dimensions shown are in inches)

Figure 4. MFFH radiation patterns at 21.0 GHz, vertical polarization, H-plane cut. (A) with original SMMR flare angle and (B) with narrower TMR flare angle. Reduced phase error at the higher frequencies lowers the ripple in the pattern and improves the impedance match,

Figure 5. Characterization of TMR radome reflections from 5/8" thick, 2 lbs/ft^3 polystyrene: Standing waves in the antenna temperature are observed as the radome is moved in front of a water vapor radiometer observing the zenith sky. The solid line is the measured antenna temperature. The dashed line is the Fourier component corresponding to the standing waves due to reflections from the radome, oscillating at one-half the RF wavelength for 20.7 GHz.

Figure 6. Model used for the radiative transfer of thermal emission through the TMR front end hardware,

Figure 7. T/V test temperature time lines for overall instrument and antenna temperature variations.

Figure 8. T/V test measured temperature variations of individual microwave components.

Figure 9. 18 GHz residual error in the T_A algorithm without a correction for instrument non-linearity

Figure 10. Dependence of quadratic non-linearity correction terms on the

instrument temperature for the 18 GHz channel,

Figure 11. Residual error in the T_A algorithm with a temperature dependent quadratic correction included for the instrument non-linearities. (A) 18GHz, (B) 21 GHz, and (C) 37 GHz.

Fig 1

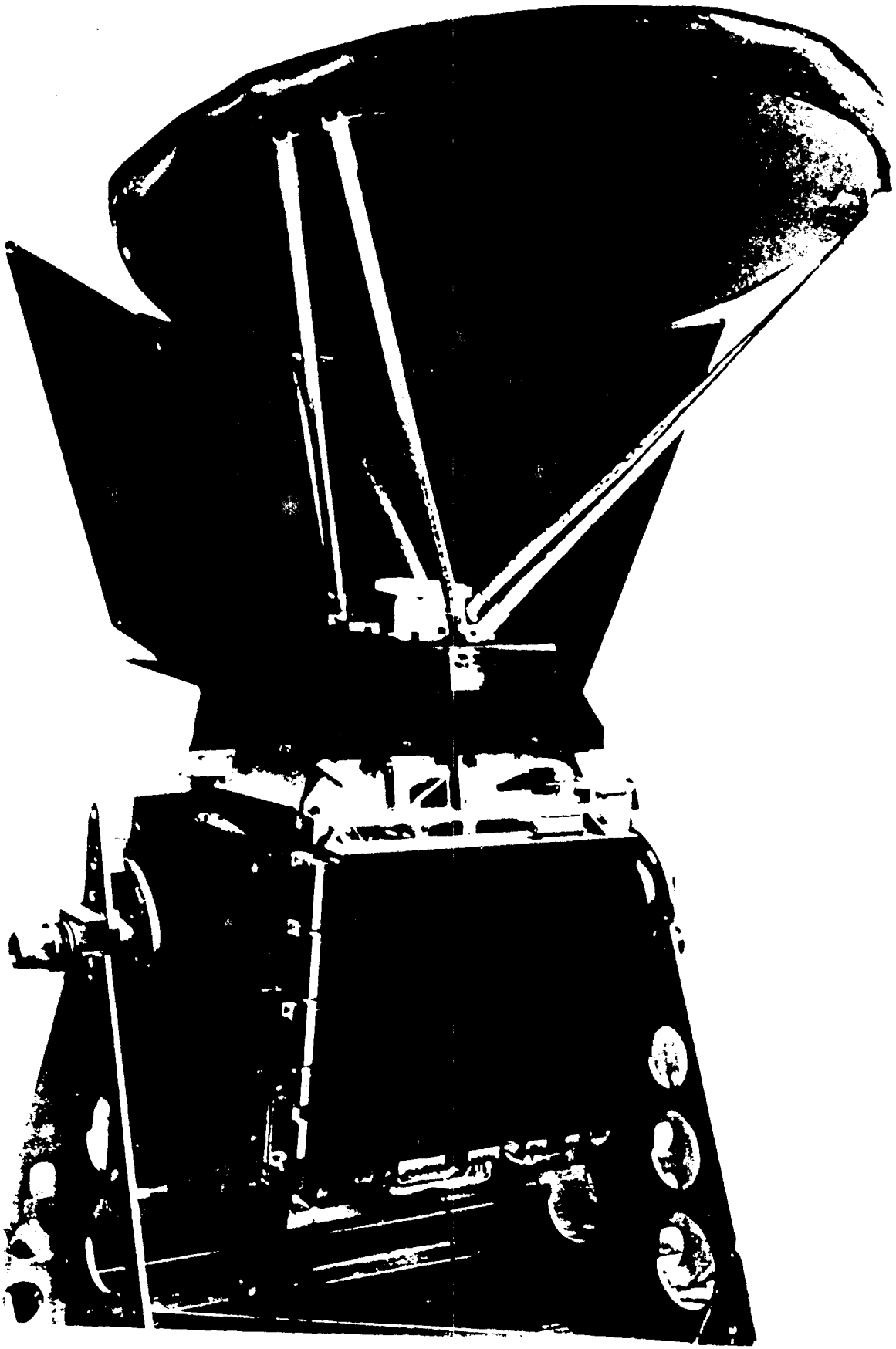

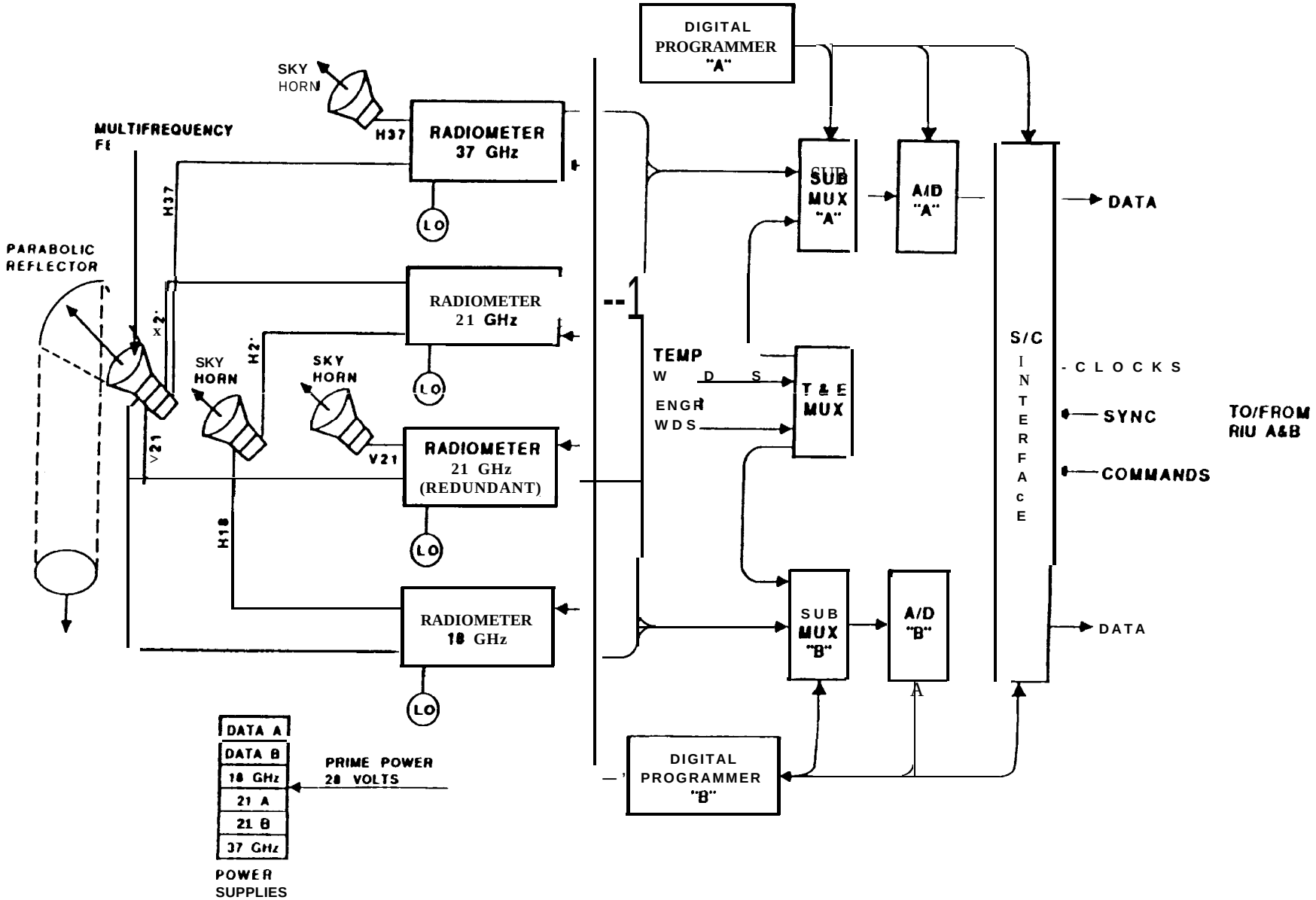
DIGITAL PROGRAMMER "A"
SKY HORN
H37
RADIOMETER 37 GHz
MULTIFREQUENCY FE
H37
LO
SUB MUX "A"
A/D "A"
DATA
PARABOLIC REFLECTOR
RADIOMETER 21 GHz
V2
H2
SKY HORN
SKY HORN
TEMP
W D S
ENGR WDS
T & E MUX
S/C INTERFACE
CLOCKS
SYNC
COMMANDS
TO/FROM RIU A&B
V21
RADIOMETER 21 GHz (REDUNDANT)
H18
SUB MUX "B"
A/D "B"
DATA
RADIOMETER 18 GHz
DATA A
DATA B
18 GHz
21 A
21 B
37 GHz
PRIME POWER 28 VOLTS
DIGITAL PROGRAMMER "B"
POWER SUPPLIES

F-5 2A

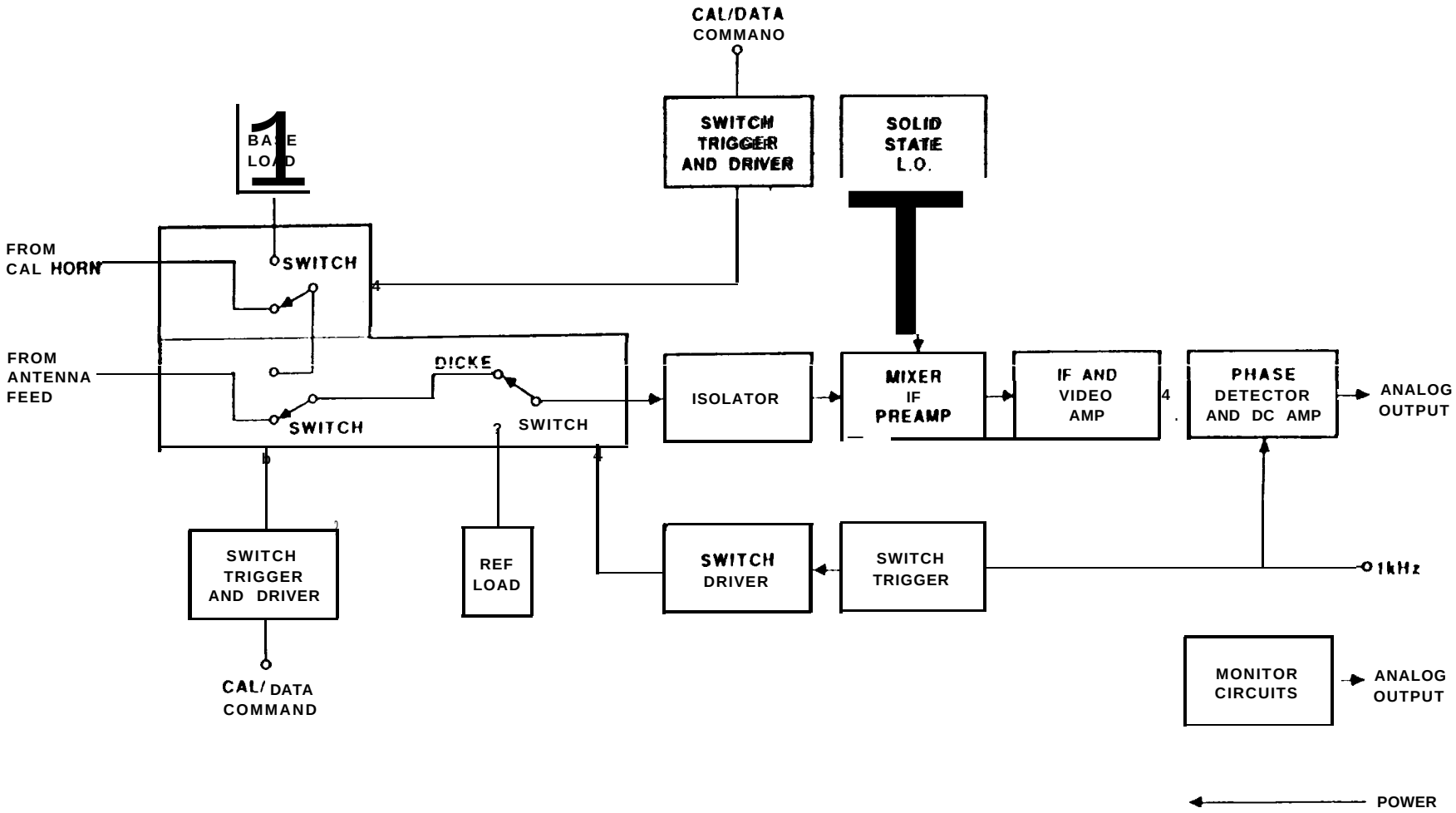
CAL/DATA
COMMANO
SWITCH
TRIGGER
AND DRIVER
SOLID
STATE
L.O.
BASE
LOAD
FROM
CAL HORN
SWITCH
FROM
ANTENNA
FEED
DICKE
SWITCH
SWITCH
ISOLATOR
MIXER
IF
PREAMP
IF AND
VIDEO
AMP
PHASE
DETECTOR
AND DC AMP
ANALOG
OUTPUT
SWITCH
TRIGGER
AND DRIVER
REF
LOAD
SWITCH
DRIVER
SWITCH
TRIGGER
1kHz
MONITOR
CIRCUITS
ANALOG
OUTPUT
CAL/DATA
COMMAND
POWER

Fig 23

Fig 3

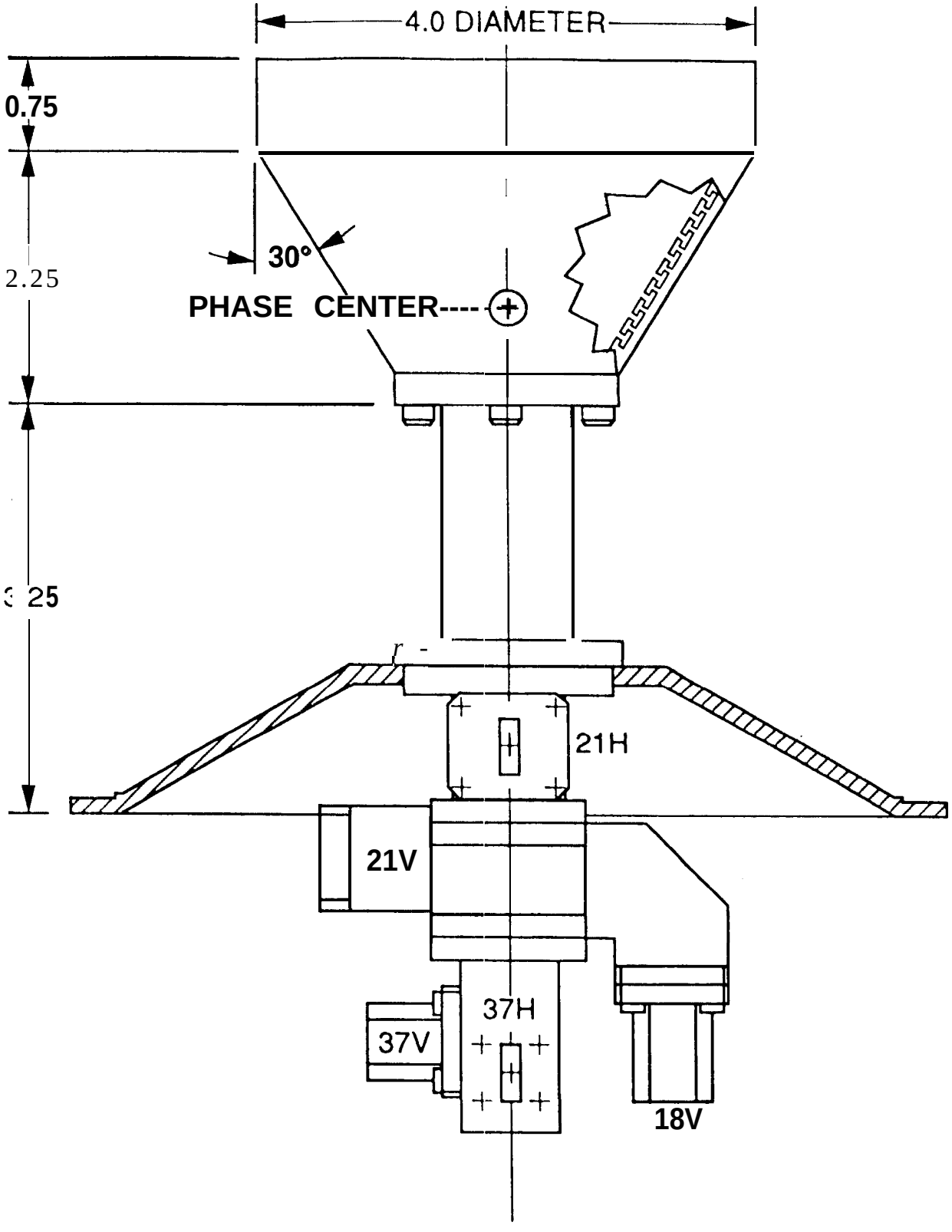

Fig 4a

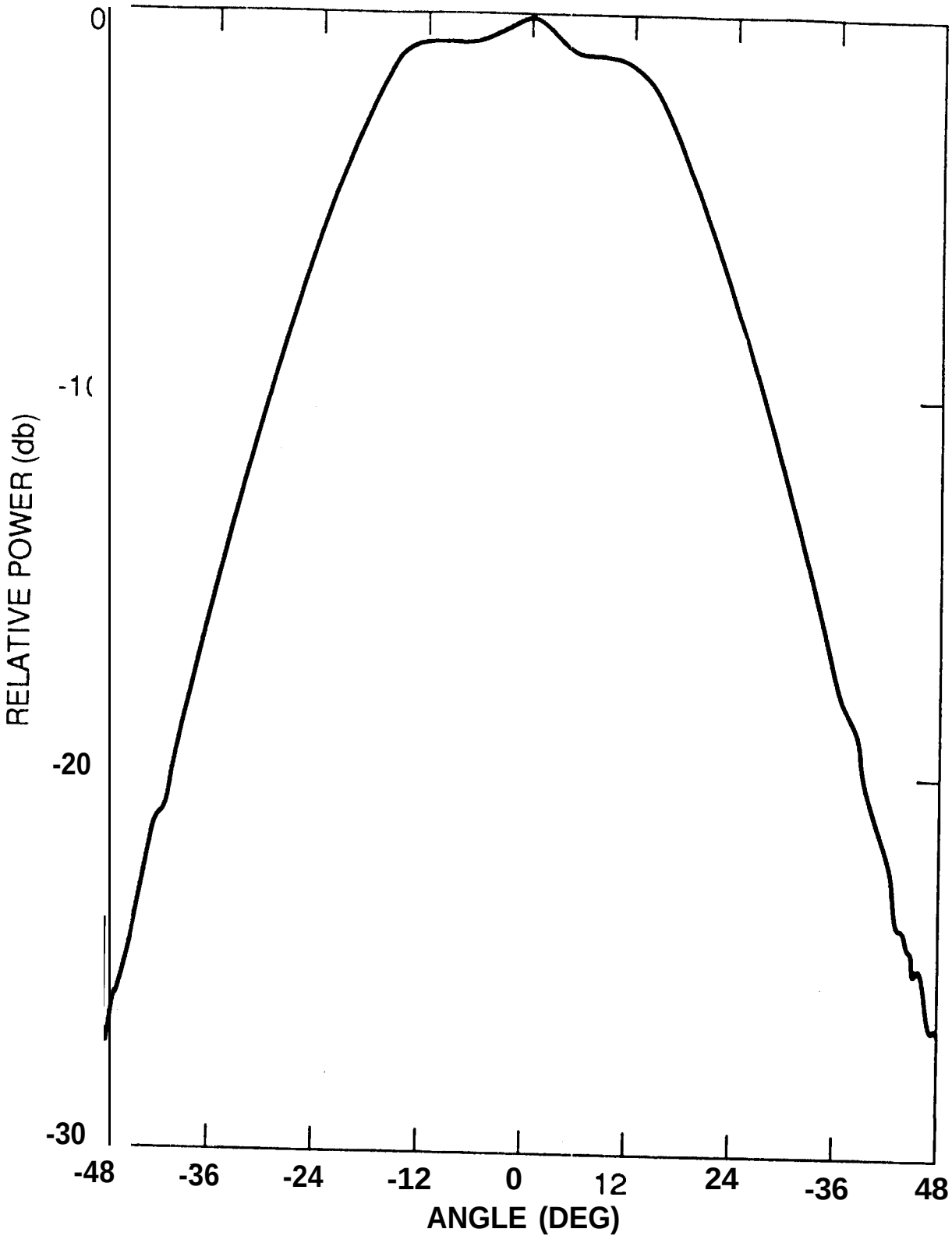

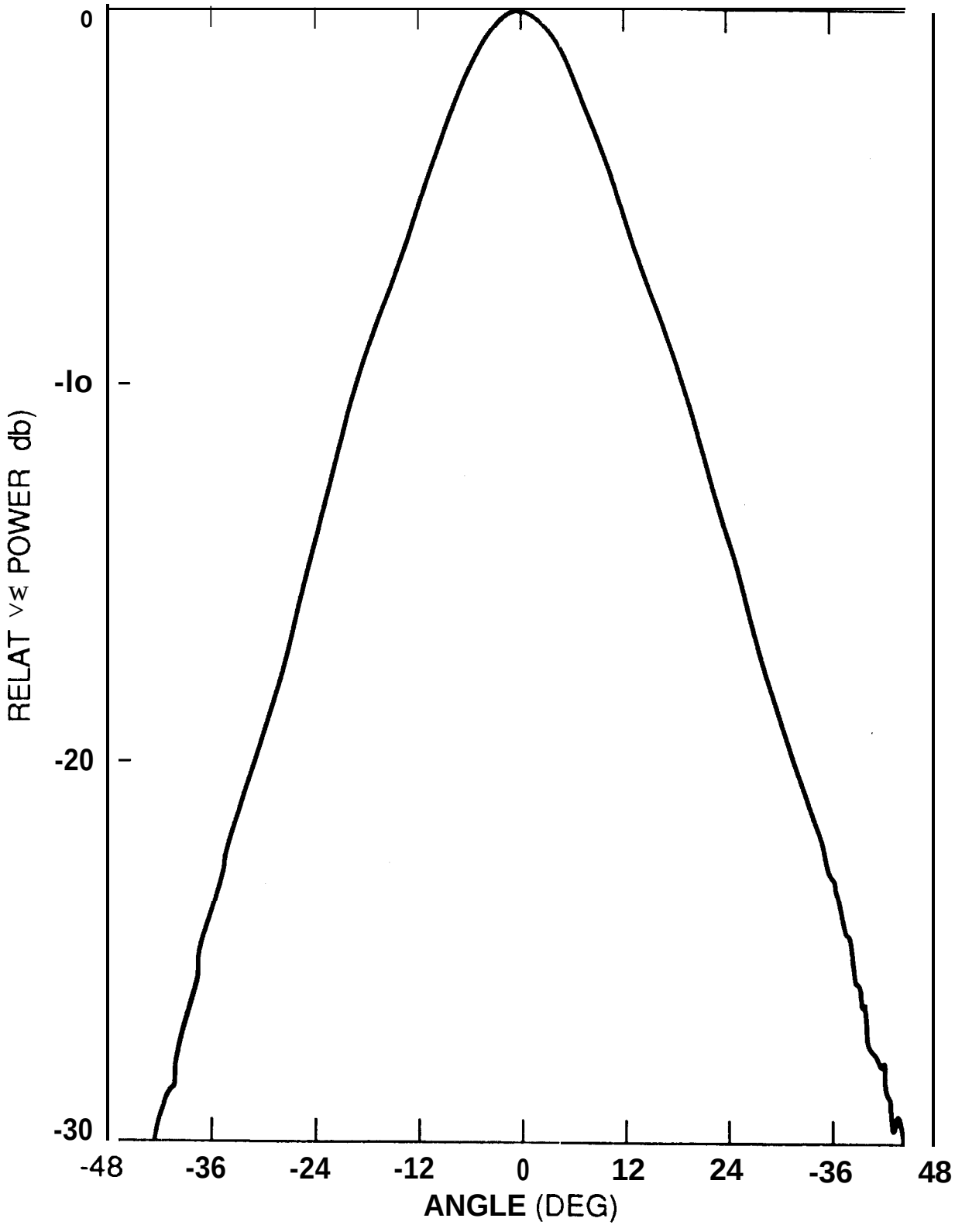
0
-Io
-20
-30
RELAT ⋎≪ POWER db)
-48
-36
-24
-12
0
12
24
-36
48
ANGLE (DEG)

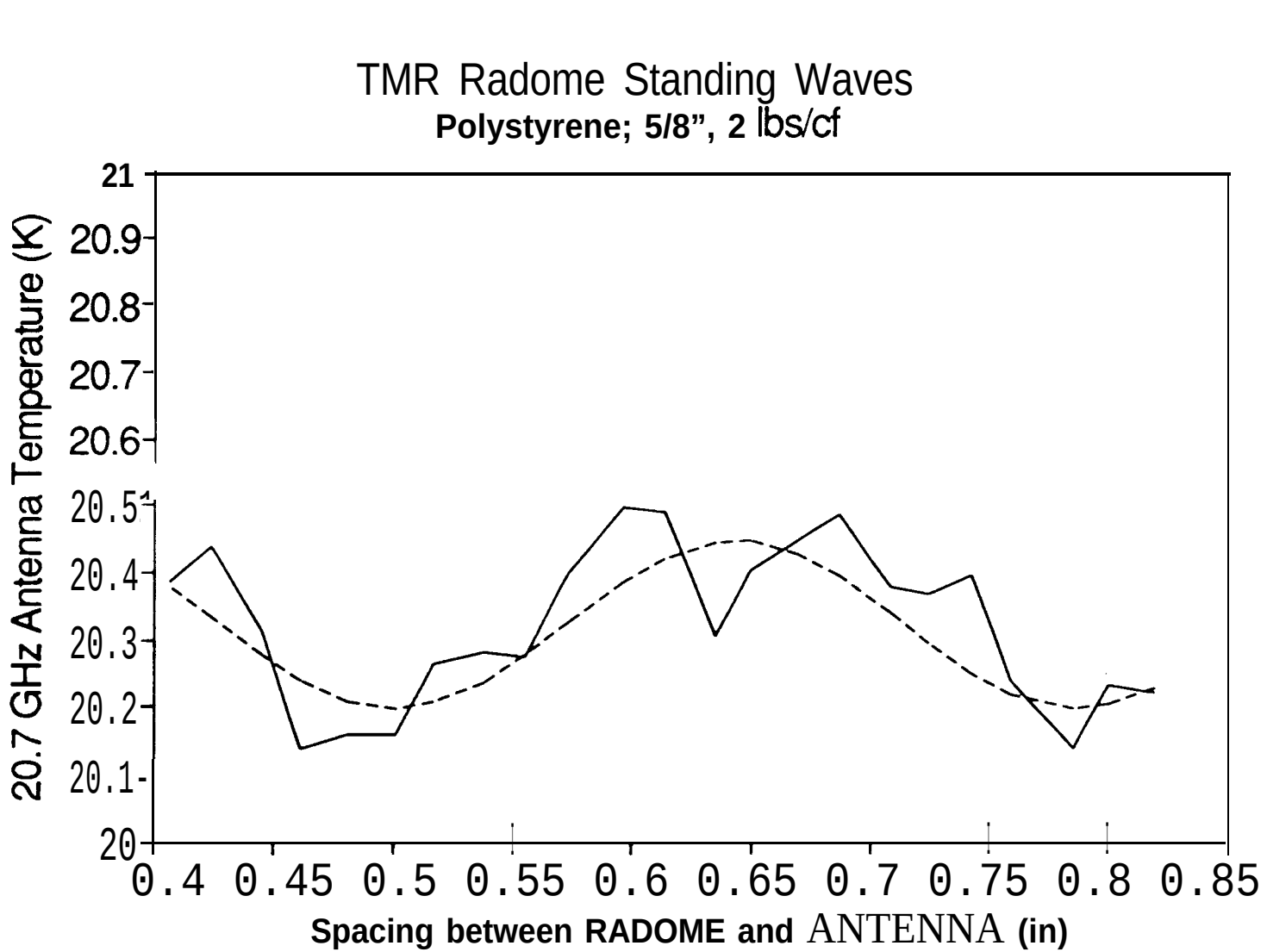
TMR Radome Standing Waves
Polystyrene; 5/8", 2 lbs/cf
20.7 GHz Antenna Temperature (K)
21
20.9
20.8
20.7
20.6
20.5
20.4
20.3
20.2
20.1
20
0.4 0.45 0.5 0.55 0.6 0.65 0.7 0.75 0.8 0.85
Spacing between RADOME and ANTENNA (in)

Fig 5

Fig 6

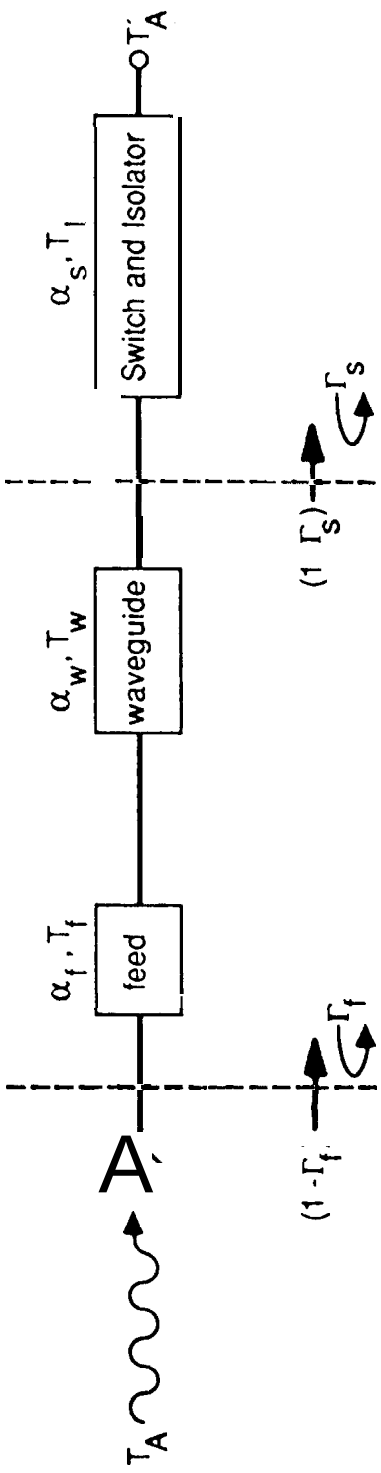

TMR Model **for Analysis of Radiative Transfer**

Fig 7

TOPEX MICROWAVE RADIOMETER
THERMAL/VACUUM TEST EVENT TIME LINE

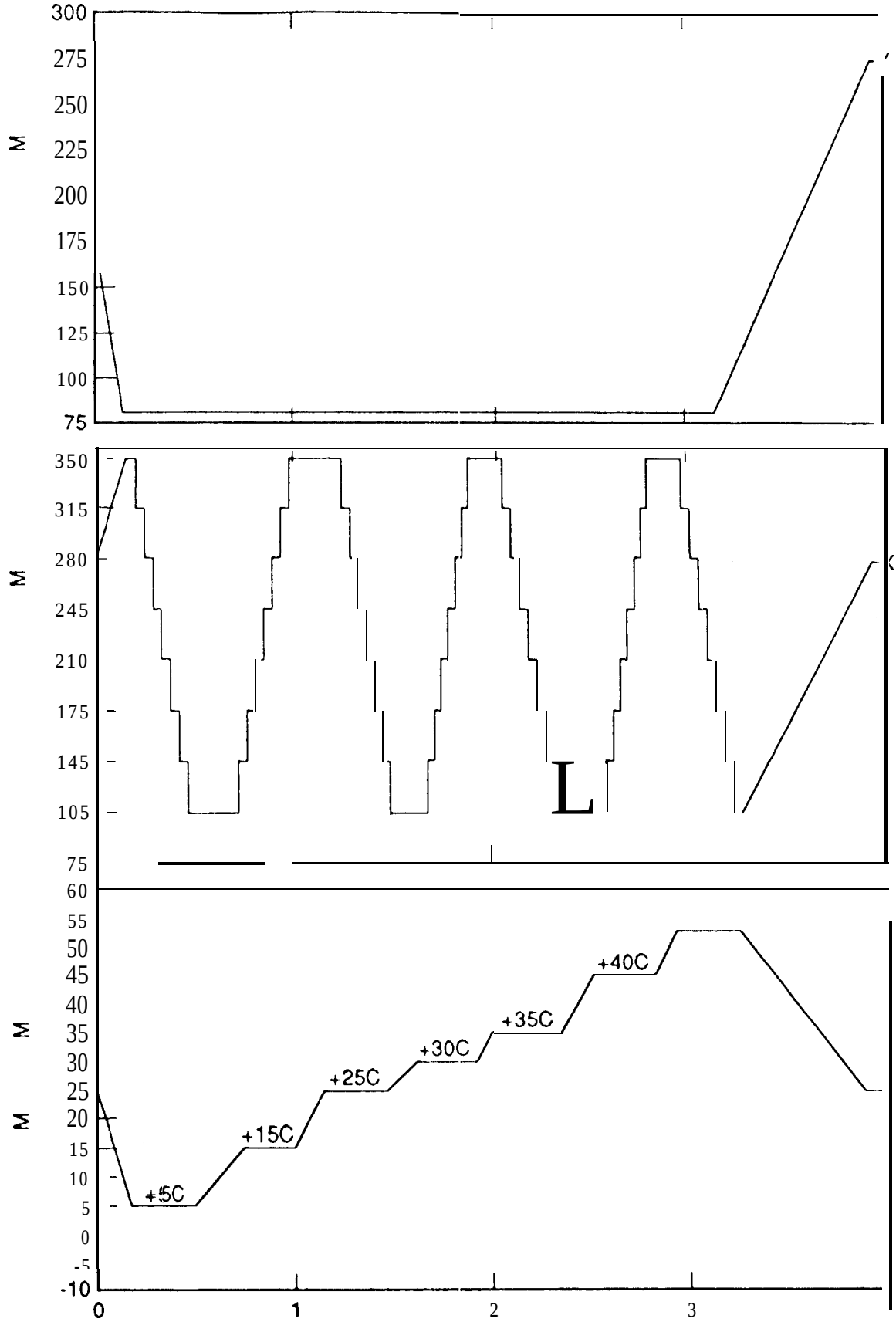

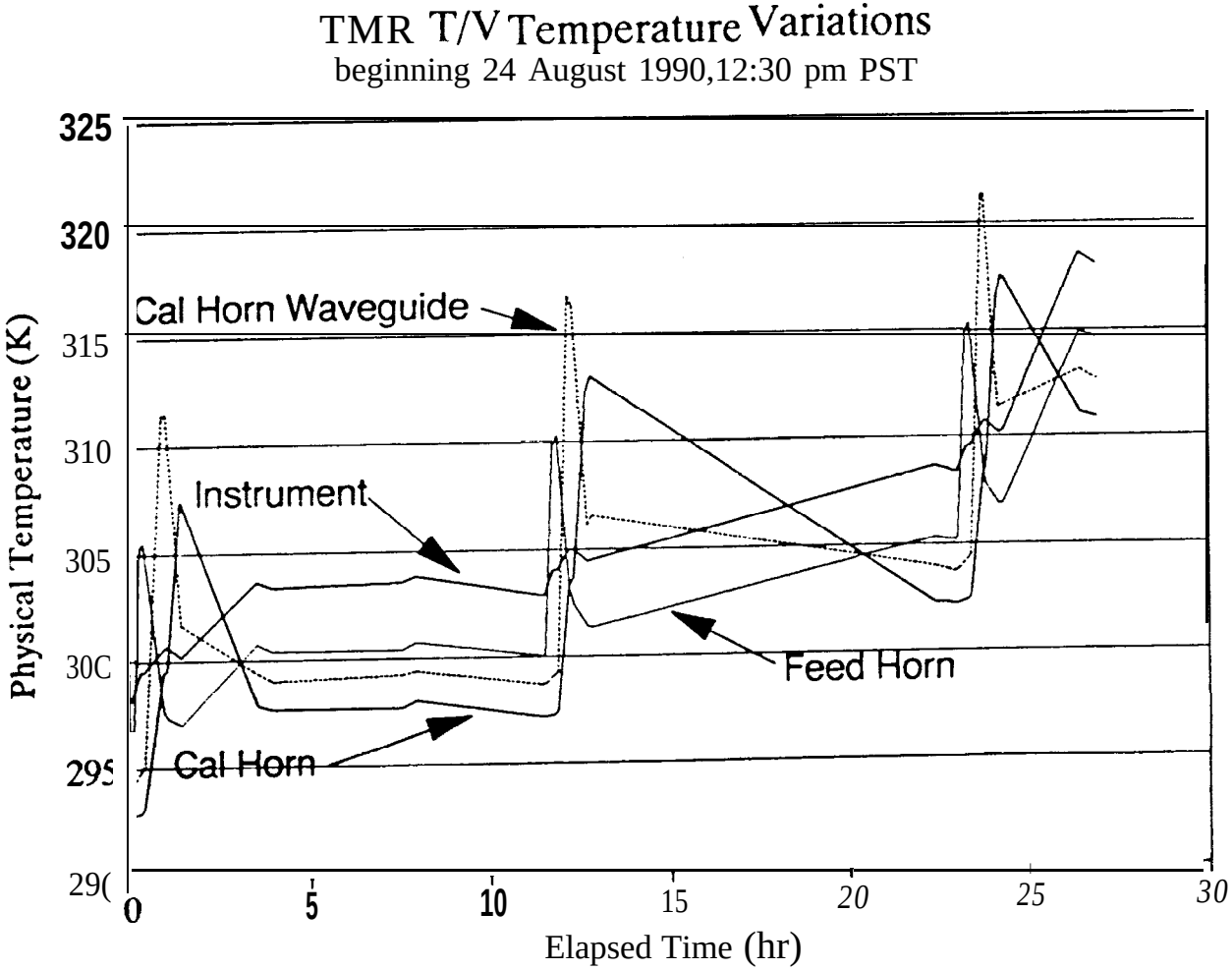
TMR T/V Temperature Variations
beginning 24 August 1990,12:30 pm PST
Physical Temperature (K)
325
320
315
310
305
30C
295
29(
Cal Horn Waveguide
Instrument
Feed Horn
Cal Horn
0
5
10
15
20
25
30
Elapsed Time (hr)

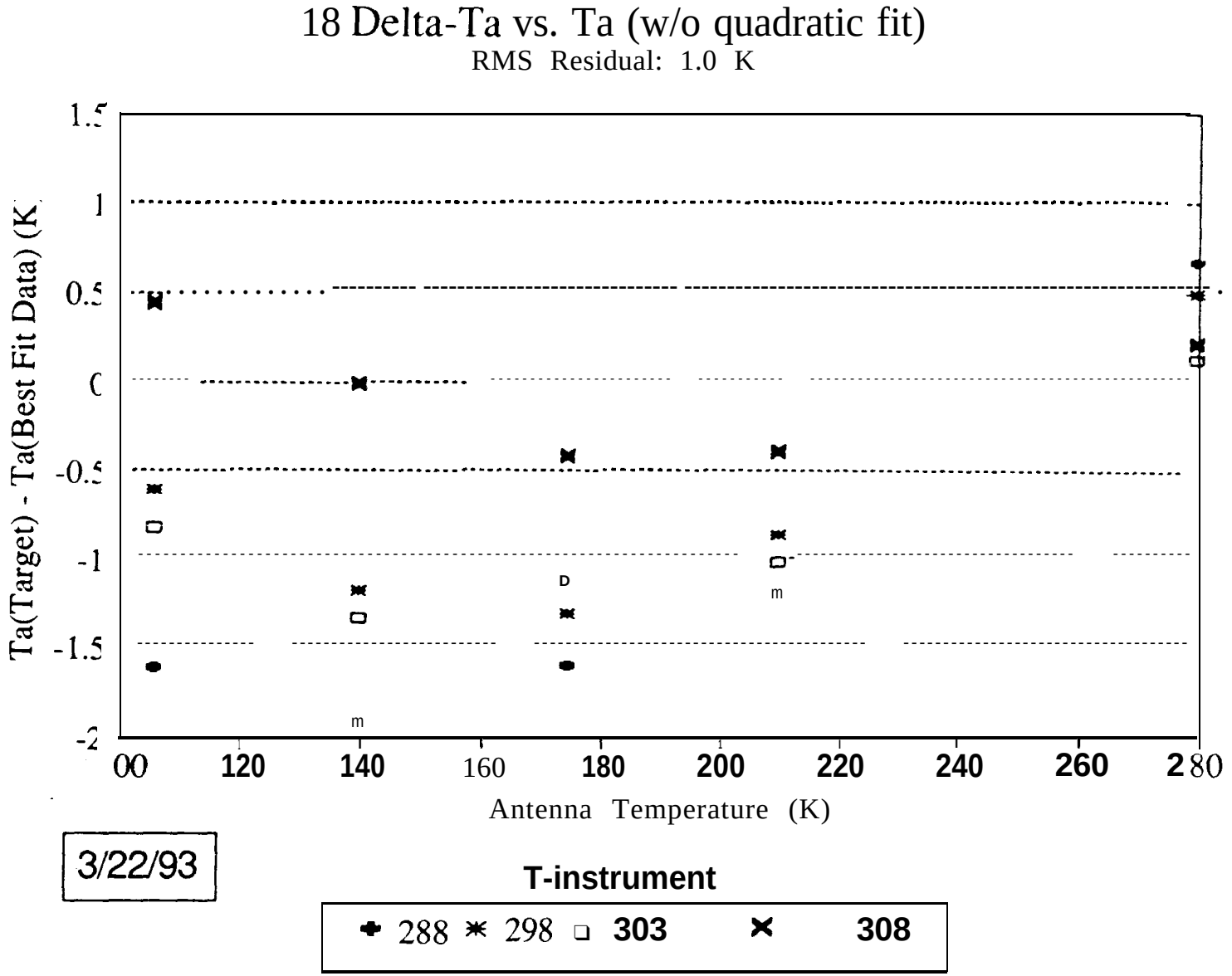
18 Delta-Ta vs. Ta (w/o quadratic fit)
RMS Residual: 1.0 K
Ta(Target) - Ta(Best Fit Data) (K
1.5
1
0.5
0
-0.5
-1
-1.5
-2
00
120
140
160
180
200
220
240
260
280
Antenna Temperature (K)
3/22/93
T-instrument
288
298
303
308

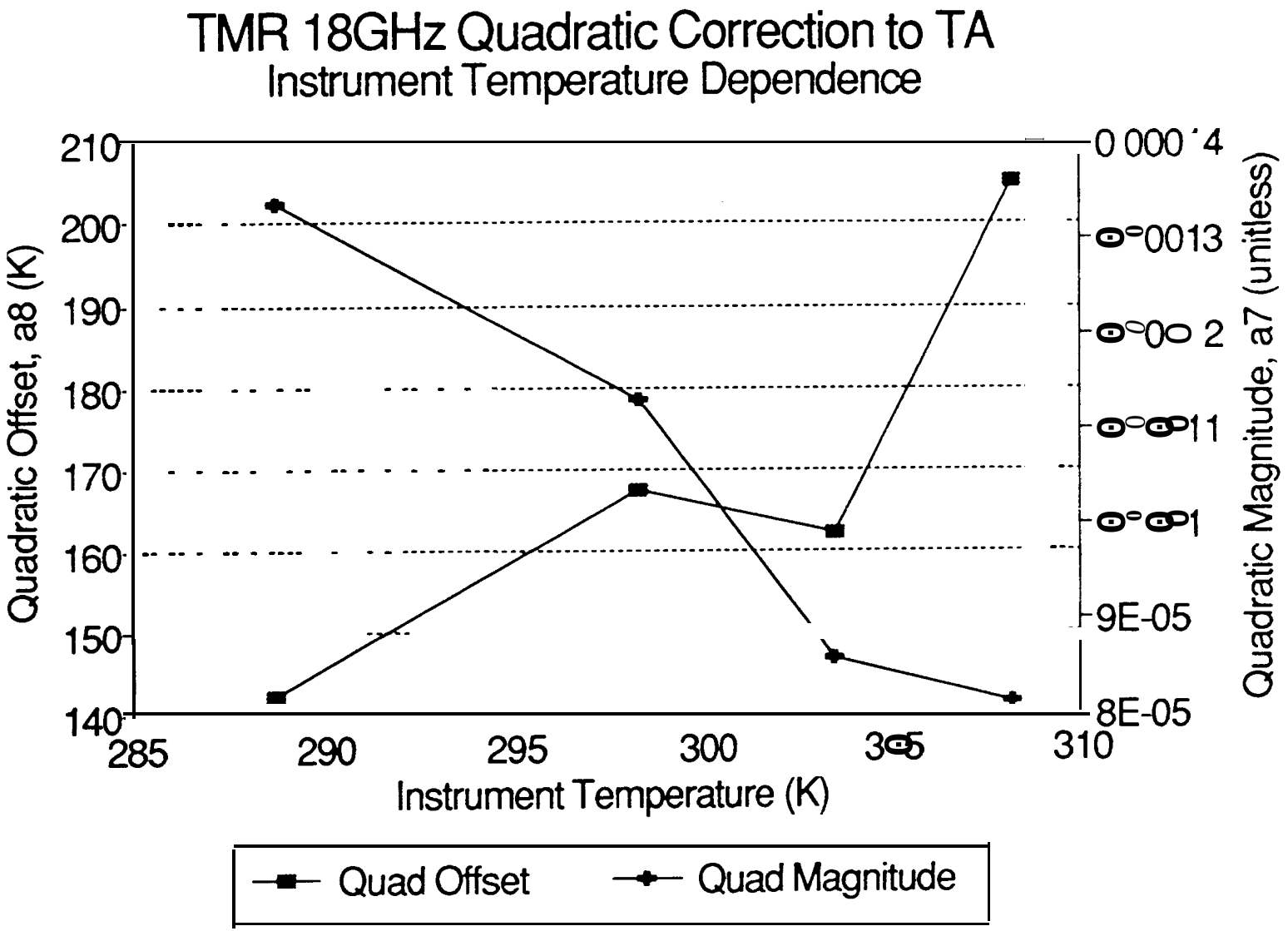
TMR 18GHz Quadratic Correction to TA
Instrument Temperature Dependence
Quadratic Offset, a8 (K)
210
200
190
180
170
160
150
140
285
290
295
300
310
Instrument Temperature (K)
Quadratic Magnitude, a7 (unitless)
0.0004
0.0013
0.002
0.0011
0.001
9E-05
8E-05
Quad Offset
Quad Magnitude

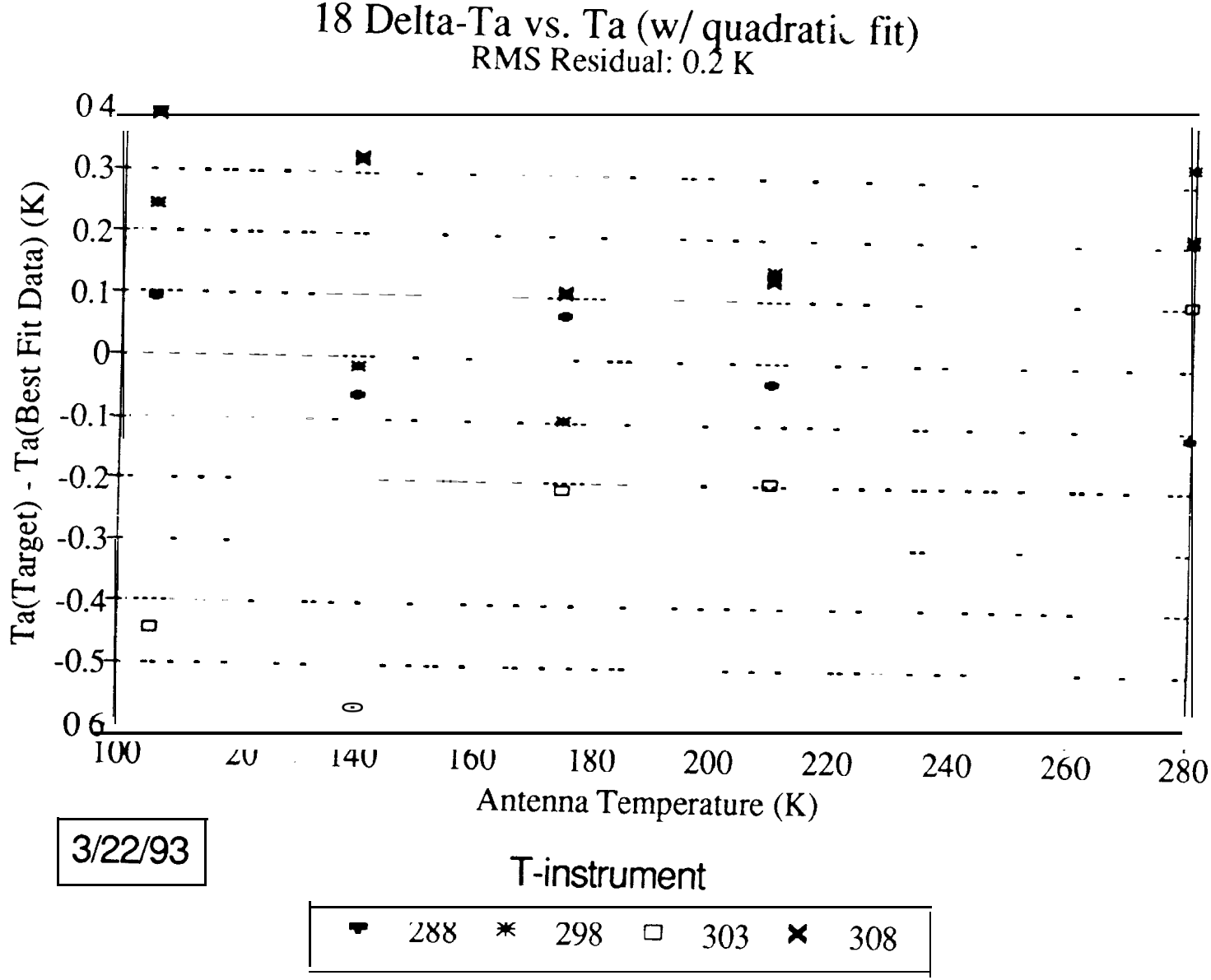
18 Delta-Ta vs. Ta (w/ quadratic fit)
RMS Residual: 0.2 K
Ta(Target) - Ta(Best Fit Data) (K)
0.4
0.3
0.2
0.1
0
-0.1
-0.2
-0.3
-0.4
-0.5
-0.6
100
120
140
160
180
200
220
240
260
280
Antenna Temperature (K)
3/22/93
T-instrument
288
298
303
308

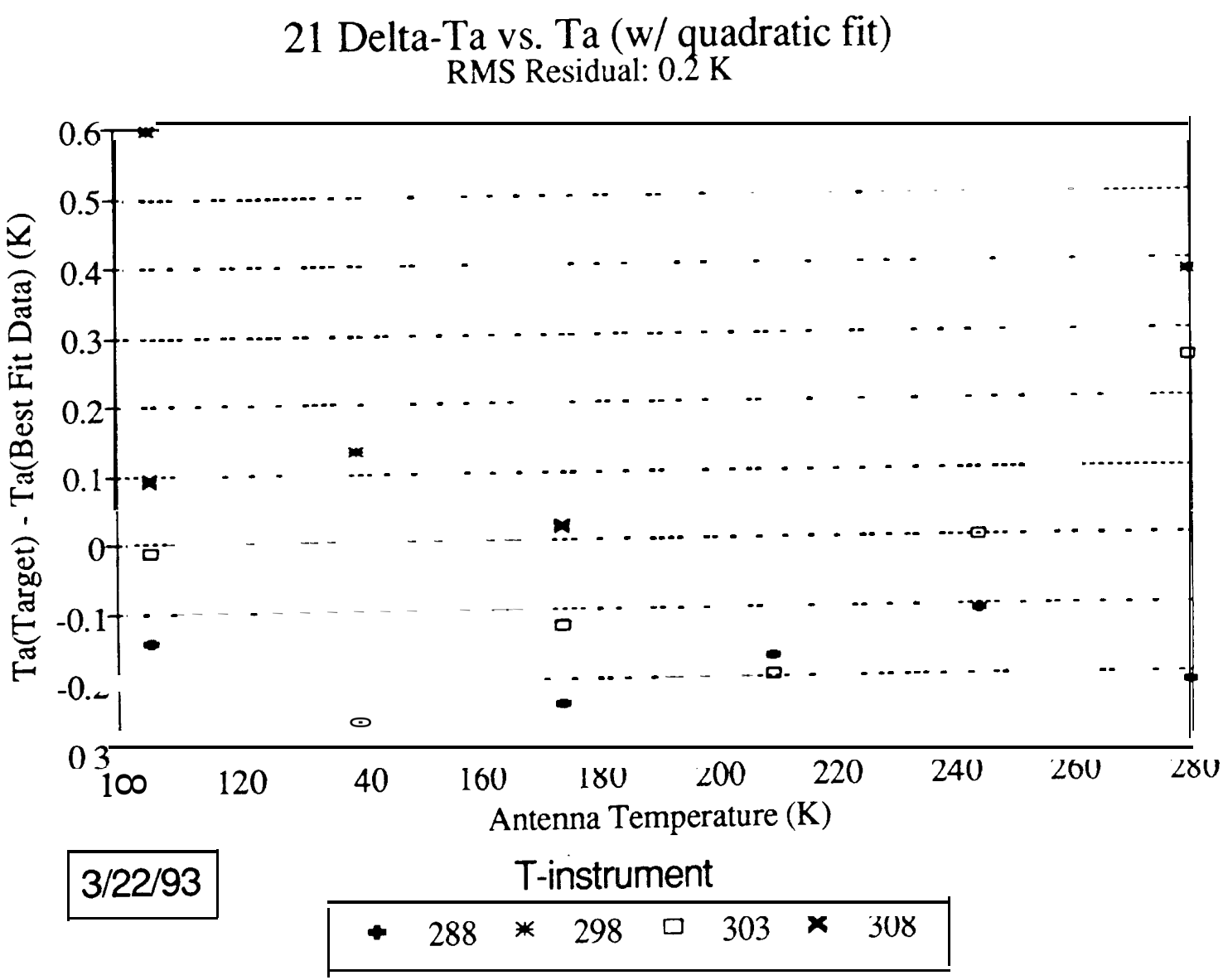
21 Delta-Ta vs. Ta (w/ quadratic fit)
RMS Residual: 0.2 K
Ta(Target) - Ta(Best Fit Data) (K)
0.6
0.5
0.4
0.3
0.2
0.1
0
-0.1
100
120
40
160
180
200
220
240
260
280
Antenna Temperature (K)
3/22/93
T-instrument
288
298
303
308

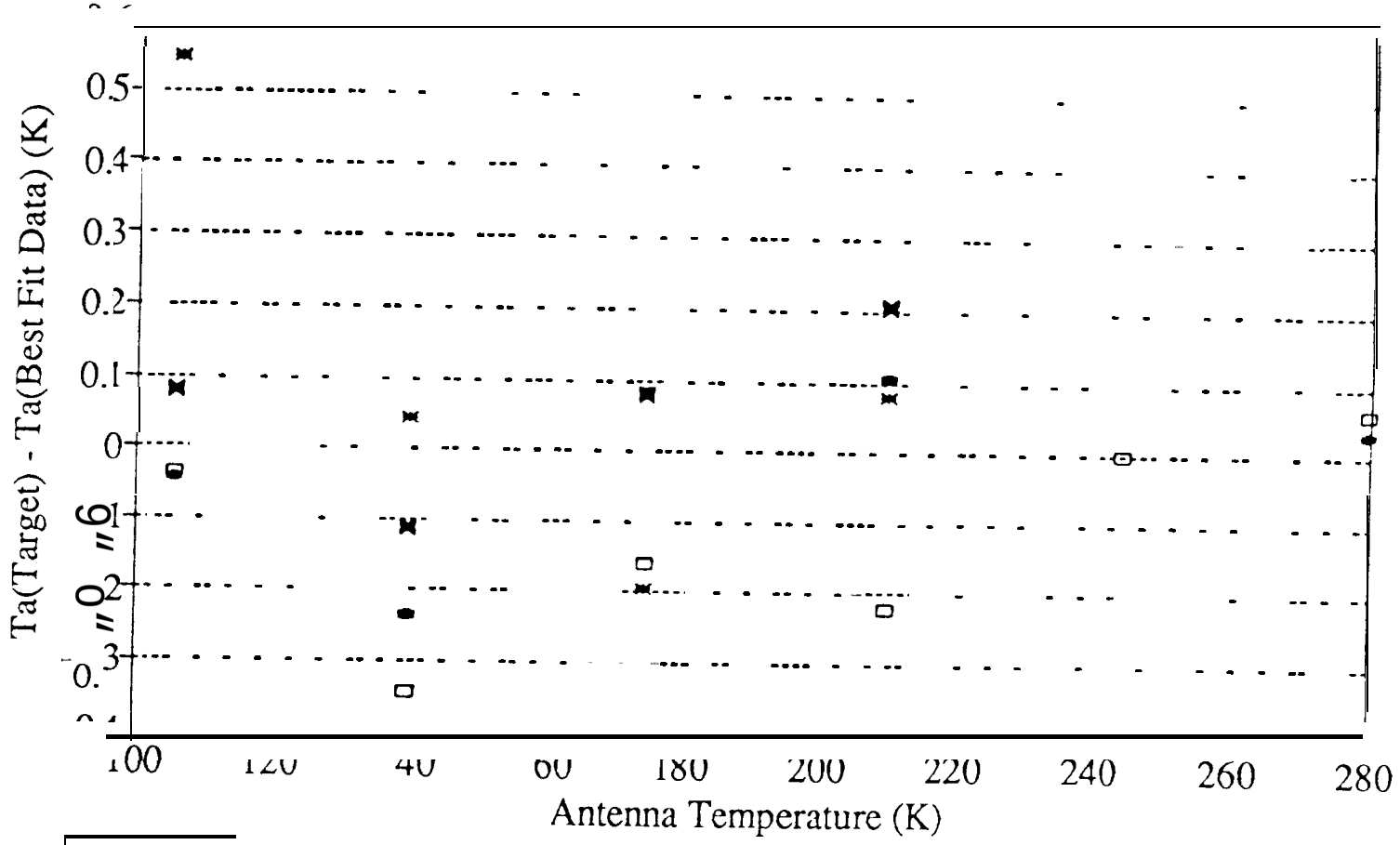
37 Delta-Ta vs. Ta (w/ quadratic fit
RMS Residual: 0.2 K
Ta(Target) - Ta(Best Fit Data) (K)
0.5
0.4
0.3
0.2
0.1
0
0.1
0.2
0.3
100
120
140
160
180
200
220
240
260
280
Antenna Temperature (K)
3/22/93
T-instrument
288
298
303
308